

1 Upper ocean temperature characteristics in the subantarctic 2 Southeast Pacific based on biomarker reconstructions

3 Julia R. Hagemann¹, Lester Lembke-Jene¹, Frank Lamy¹, Maria-Elena Vorrath², Jérôme Kaiser³, Juliane
4 Müller¹, Helge W. Arz³, Jens Hefter¹, Andrea Jaeschke⁴, Nicoletta Ruggieri¹, Ralf Tiedemann¹

5 ¹Alfred Wegener Institute, Helmholtz Centre for Polar and Marine Research, 27570 Bremerhaven, Germany

6 ²Institute for Geology, University Hamburg, 20146 Hamburg, Germany

7 ³Leibniz-Institute for Baltic Sea Research Warnemünde, 18119 Rostock, Germany

8 ⁴Institute of Geology and Mineralogy, University of Cologne, 50923 Cologne, Germany

9

10 *Correspondence to:* Julia. R. Hagemann (Julia.Hagemann@awi.de) and Lester Lembke-Jene (Lester.Lembke-Jene@awi.de)

11 **Abstract.** Alkenones and isoprenoid Glycerol Dialkyl Glycerol Tetraether lipids (isoGDGT) as remnants of living organisms
12 are widely used biomarkers for determining past oceans' water temperatures. The organisms these proxy carriers stem from,
13 are influenced by a number of environmental parameters, such as water depth, nutrient availability, light conditions or
14 seasonality, which all may significantly bias the calibration to ambient water temperatures. Reliable temperature
15 determinations remain thus challenging, especially in higher latitudes and for under-sampled regions. We analyzed 33 sediment
16 surface samples from the Southern Chilean continental margin and the Drake Passage for alkenones and isoGDGTs and
17 compared the results with gridded instrumental reference data from the World Ocean Atlas 2005 (WOA05), as well as
18 previously published data from an extended study area covering the Central and Western South Pacific towards the New
19 Zealand continental margin. We show that for alkenone-derived Sea Surface Temperatures (SST), the widely-used global core-
20 top calibration of Müller et al. (1998) yields the smallest deviation of the WOA05-based SSTs. The calibration of Sikes et al.
21 (1997) instead, adapted to higher latitudes and supposed to show summer SSTs, overestimates modern WOA05-based SSTs.
22 Our alkenone SSTs show a slight seasonal shift of $\sim 1^\circ\text{C}$ at the Southern Chilean Margin and up to $\sim 2^\circ\text{C}$ in the Drake Passage
23 towards austral summer SSTs. Samples in the Central South Pacific on the other hand reflect an annual mean signal. We show
24 that for isoGDGT-based temperatures the subsurface calibration of Kim et al. (2012a) best reflects temperatures from the
25 WOA05 in areas north of the Subantarctic Front (SAF). Temperatures south of the SAF in contrast are significantly
26 overestimated by up to 14°C , irrespective of the applied calibration. In addition, we used the GDGT [2]/[3]-ratios, which gives
27 an indication of the production depth of the isoGDGTs and/or potentially influences from land. Our samples reflect a
28 subsurface (0 to 200 m water depth) rather than a surface (0 – 50 m water depth) signal in the entire study area and show a
29 correlation with the monthly dust distribution in the South Pacific, indicating terrigenous influences. The overestimation of
30 isoGDGTs surface and subsurface temperatures south of the SAF highlights the need for a re-assessment of existing
31 calibrations in the polar Southern Ocean. Therefore, we suggest a modified Southern Ocean TEX^L₈₆ – based calibration for

32 surface and subsurface temperatures, which shows a lower temperature sensitivity and yields principally lower absolute
33 temperatures, which align more closely with WOA05-derived values and also OH-isoGDGT-derived temperatures.

34 **1 Introduction**

35 Alkenones (e.g., Brassell et al., 1986; Herbert, 2001, 2014) and isoGDGTs (isoprenoid Glycerol Dialkyl Glycerol Tetraether;
36 Schouten et al., 2002; Schouten et al., 2013a) are widely used for determining oceans' past water temperatures. These
37 biomarkers are present in all oceans and occur from the tropics to high latitudes (e.g., Herbert et al., 2010; Sikes et al., 1997;
38 Müller et al., 1998; Conte et al., 2006). Alkenone-derived sea surface temperatures (SSTs) are based on lipid remains of
39 photoautotrophic Coccolithophorids (e.g., Baumann et al., 2005; Brassell et al., 1986). The ratio of di- and tri-unsaturated
40 alkenones, expressed as the Unsaturation Ketone index U^{K}_{37} (**Table A1**) is reflecting SSTs (Prahl and Wakeham, 1987).
41 Calculation of SSTs is based on calibration equations developed over the past ~40 years (**Table A1**). Most of these empirically-
42 derived equations are relatively similar, and based on comparison of either culture experiments (Prahl et al., 1988; Prahl and
43 Wakeham, 1987) or surface sediment samples from tropical to subpolar regions with corresponding instrumental data (Müller
44 et al., 1998). Other calibrations (e.g., Sikes et al., 1997) were developed specifically for (sub)polar regions and are adapted for
45 a seasonal bias toward summer SSTs. Henceforth, we use the terms Müller98 for the calibration by Müller et al. (1998) and
46 Sikes97 for the calibration by Sikes et al. (1997; **Table A1**).

47 The accuracy of alkenone-based calibrations can be influenced by other environmental factors besides temperature, such
48 as light levels, changes in growth rate or nutrient availability, but none of these factors seems to have an appreciable effect on
49 the U^{K}_{37} index (e.g., Caniupán et al., 2014; Epstein et al., 2001; Herbert, 2001; Müller et al., 1998; Popp et al., 1998). In
50 contrast, preferential degradation of the alkenone $C_{37:3}$ in sediment under aerobic conditions may bias the U^{K}_{37} signal towards
51 warmer SSTs (Prahl et al., 2010). Seasonality often plays a significant role at high latitudes (e.g., Max et al., 2020; Prahl et al.,
52 2010), due to primary production being more pronounced in the thermal summer season and annual temperature differences
53 that increases with increasing latitude. In our study region, samples from the Central South Pacific most likely represent either
54 summer temperatures (with the Sikes97 calibration) or an annual mean (Müller98 calibration; Jaeschke et al., 2017). Prahl et
55 al. (2010), using samples from the Chilean continental slope, found a slight seasonal summer bias south of ~50° S. In contrast,
56 studies from the North Pacific show a seasonal signal towards late summer to autumn SSTs that differ from the annual mean
57 by up to 6° C (e.g., Max et al., 2020; Prahl et al., 2010).

58 IsoGDGTs are lipid remains of *Thaumarchaeota* (formerly called Crearchaeota Group I; Brochier-Armanet et al., 2008)
59 that include a certain number of moieties, which increases with growth temperature (Schouten et al., 2002). The lipids GDGT-
60 0; GDGT-1; GDGT-2; GDGT-3 contain zero to three cyclopentane moieties in their molecule structure, whereas Crenarchaeol
61 and its isomer Cren' feature four cyclopentane and one hexane moieties. These ring structures regulate membrane fluidity of
62 *Thaumarchaeota* and change as an adaption to their ambient temperature (Chong, 2010; Gabriel and Chong, 2000; Schouten
63 et al., 2002). Determination of isoGDGT-derived water temperatures is based on the Tetraether index (TEX₈₆; Schouten et al.,

64 2002), or their modifications $\text{TEX}^{\text{H}}_{86}$ and $\text{TEX}^{\text{L}}_{86}$ (**Table A1**), which have been determined for water temperatures $>15^\circ\text{C}$ and
65 $<15^\circ\text{C}$, respectively (Kim et al., 2010). While $\text{TEX}^{\text{H}}_{86}$ is a logarithmic function of the original index, $\text{TEX}^{\text{L}}_{86}$ omits the GDGT-
66 3 from the denominator and removes the isomer Cren' from the equation, due to a weaker correlation to water temperatures in
67 cold regions (Kim et al., 2010). In addition to cyclopentane moieties, three OH-isoGDGTs may also contribute to ambient
68 temperature adaption (OH-isoGDGT-0, OH-isoGDGT-1, and OH-isoGDGT-2). These OH-isoGDGTs occur globally, but in
69 higher amounts in the polar regions, as further adaption of the *Thaumarchaeota* to the cold environment (Fietz et al., 2013;
70 Huguet et al., 2013; Liu et al., 2020). OH-isoGDGTs are frequently so important in polar regions or during glacial phases that
71 it has been recommended to include them in temperature calibrations (Fietz et al., 2020; Fietz et al., 2016). In contrast to photo-
72 autotrophic coccolithophores, *Thaumarchaeota* occur throughout the water column (Karner et al., 2001), which complicates
73 the attribution of the reconstructed temperature signal to specific water depths. In general, it is assumed that *Thaumarchaeota*
74 predominantly reflect either a subsurface, i.e., seasonal mixed-layer temperature (T_{sub} ; 0 – 200 m water depth), or an SST
75 signal (**Table A1**), because the grazing and repacking of isoGDGTs into fecal pellets occurs most effectively within the photic
76 zone (Wuchter et al., 2005). The GDGT [2]/[3]-ratio can be used to roughly determine the habitat depth of the
77 *Thaumarchaeota*, since it increases with increasing water depth (Dong et al., 2019; Hernández-Sánchez et al., 2014; Kim et
78 al., 2015; Kim et al., 2016; Schouten et al., 2012; Taylor et al., 2013). For the subpolar and polar Southern Ocean, in particular
79 the extensive SE Pacific sector, only little information exists to date about the applicability of these different temperature
80 proxies and their respective calibrations. In addition, systematic comparisons between alkenone and isoGDGT-based
81 temperature reconstructions using surface sediments have thus far been limited (e.g., Jaeschke et al., 2017; Kaiser et al., 2015).
82 We use the terms $\text{SST}^{\text{H}}_{\text{Kim}}$ and $\text{SST}^{\text{L}}_{\text{Kim}}$ for the two global surface calibrations by Kim et al. (2010), $T_{\text{sub}}^{\text{H}}_{\text{Kim}}$ and
83 $T_{\text{sub}}^{\text{L}}_{\text{Kim}}$ for the two global subsurface calibrations by Kim et al. (2012a, 2012b) and $\text{SST}^{\text{H}}_{\text{Kaiser}}$ and $T_{\text{sub}}^{\text{H}}_{\text{Kaiser}}$ for the
84 local surface and subsurface calibration by Kaiser et al. (2015; **Table A1**).

85 In this study, we present a new set of 33 sediment surface samples located along the Southern Chilean Margin (SCM) and
86 the Drake Passage (DP; $\sim 52 - 62^\circ\text{S}$) to determine upper ocean water temperatures based on alkenones (U^{K}_{37}) and isoGDGTs
87 ($\text{TEX}^{\text{H}}_{86}$ and $\text{TEX}^{\text{L}}_{86}$). We compare our regional results with previously published data from an extended, temperate to subpolar
88 South Pacific study area (**Figure 1**).

89 We assess the applicability of the Müller98 and Sikes97 calibrations with World Ocean Atlas (WOA05)-based temperatures
90 and investigate the influence of seasonality on alkenone-based temperature reconstructions. Furthermore, we compare the
91 isoGDGT-based indices $\text{TEX}^{\text{H}}_{86}$ and $\text{TEX}^{\text{L}}_{86}$ and their most common calibrations for SST and T_{sub} (**Table A1**) with WOA05-
92 based temperatures. Lastly, we check the potential influence of habitat depth on signal incorporation on the basis of the GDGT
93 [2]/[3]-ratio and propose a new calibration specifically for the polar Pacific sector of the Southern Ocean (SO) south of the
94 Subantarctic Front.

95 2 Study Area

96 Our study area comprises the subpolar and polar SE Pacific sector of the SO, including the Drake Passage (**Figure 1**). One
97 important characteristic of the SO is the eastward-flowing Antarctic Circumpolar Current (ACC), which is largely driven by
98 Southern Westerly Winds (SWW) and buoyancy forcing (Rintoul, 2018; Watson et al., 2015). The ACC flows unimpeded
99 around Antarctica, and is only slowed down by the South American continent (Orsi et al., 1995), where the northern branch of
100 the ACC bifurcates at $\sim 40 - 45^\circ$ S into the northward-flowing Peru-Chile Current (PCC) and the southward-flowing Cape
101 Horn Current (CHC; Strub et al., 1998). CHC and ACC jointly transport ca. 130 – 150 Sv of water (e.g., Koenig et al., 2014)
102 through the ~ 800 km wide Drake Passage into the Atlantic Ocean (**Figure 1**).

103 Several fronts within the ACC characterize the convergence of water masses that differ in temperature, salinity and nutrient
104 content (Orsi et al., 1995). The northern boundary of the ACC is defined by the Subtropical Front (STF; Orsi et al., 1995),
105 followed from north to south by the Subantarctic Front (SAF), the Polar Front (PF) and the Southern ACC Front (SACCF).
106 Apart from the STF, which is interrupted by the South American continent, all three fronts (SAF, PF and SACCF) pass through
107 the Drake Passage (Orsi et al., 1995; **Figure 1**). The zones between the fronts are defined as areas with differing temperature
108 and salinity characteristics, both decreasing with increasing latitude. The SAF marks the beginning of the Antarctic
109 Intermediate Water's (AAIW) northward descent to a depth of ~ 500 m. AAIW itself is associated with a salinity minimum of
110 < 34 PSU. The PF, on the other hand, marks the northern temperature limit of the cold Antarctic surface water. The SACCF
111 instead has no distinct separating features in the surface water. The boundary is here defined along the mesopelagic temperature
112 maximum of the upwelled Upper Circumpolar Deep Water (UCDW; Orsi et al., 1995 and references therein).

113 3 Material and Methods

114 A total amount of 33 Multi-Corer (MUC) samples (**Table A2**) along the Southern Chilean Margin and the Drake Passage were
115 analyzed for alkenones and isoGDGTs. The samples were collected during R/V Polarstern expedition PS97 in February-April
116 2016 (Lamy, 2016) along a latitudinal transect on the Southern Chilean Margin and through the Southern Ocean frontal system.

117 The MUC samples were stored deep-frozen immediately after sampling onboard and freeze-dried afterwards in the
118 laboratory. Extraction of the biomarkers was carried out with two different approaches. Between 3 and 5 g of ground surface
119 sediment (0 – 1 cm) from each site was extracted either by an accelerated Solvent Extraction (DIONEX ASE 350; Thermo
120 Scientific) with DCM:MeOH (9:1, v:v) for the samples of the Chilean margin (including three samples from the Drake Passage)
121 or in an ultrasonic bath with DCM:MeOH (2:1, v:v) for the samples of the Drake Passage. As internal standard, 100 μ l each
122 of the *n*-alkane C₃₆ or 2-nonadecanone standard and C₄₆ were added before extraction. The two data sets were initially used to
123 address differing research objectives. The samples from the Chilean margin (including three DP samples) were primarily used
124 for extracting alkenones for SST. Previous works on the DP samples, on the other hand, focused on highly branched
125 isoprenoids (HBIs), sterols and isoGDGTs (Lamping et al., 2021; Vorrath et al., 2020), and were extracted using sonication as
126 a lower recovery of higher unsaturated HBIs is known when using the ASE method (Belt et al., 2014). In contrast, the TEX₈₆

127 index does not appear to be substantially affected by extraction techniques (Schouten et al., 2013b). The good agreement
128 between the three ASE extraction DP samples and the ultrasonic bath samples (**Figure 7D – F**) suggests that the two data sets
129 are comparable.

130 The bulk of the solvent was removed by rotary evaporation, under a nitrogen gas stream or in a Rocket Evaporator (Genevac
131 – SP Scientific). The different fractions were chromatographically separated using small glass columns filled with 5 cm of
132 activated silicagel. After adding the sample, the column was rinsed with 5 ml *n*-hexane, 5 ml or 8 ml *n*-hexane:DCM (1:1,
133 v:v), 5 ml DCM and 4 ml DCM:MeOH (1:1, v:v) to yield *n*-alkanes, alkenones and isoGDGTs, respectively. The samples
134 were dried again and transferred into 2 ml vials. For the measurement, the alkenone fractions were diluted with 200 – 20 μ l *n*-
135 hexane, the GDGT fraction was filtered first, and then diluted with 50 – 120 μ l *n*-hexane:isopropanol (99:1, v:v).

136 Alkenones were injected with 1 μ l solvent and Helium as carrier gas into an Agilent HP6890 Gas Chromatograph equipped
137 with a 60 m DB-1 MS column and a flame ionization detector. The oven temperature was increased from initially 60° C to
138 150° C with 20° C min⁻¹ and thereafter with 6° C min⁻¹ until 320° C were reached.

139 For the GDGT measurements of most DP samples, we refer to the original studies by Lamping et al. (2021) and Vorrath et
140 al. (2020). The other part of the GDGT samples were analyzed on an Agilent 1260 Infinity II ultrahigh-performance liquid
141 chromatography-mass spectrometry (UHPLC-MS) system and a G6125C single quadrupole mass spectrometer. The
142 chromatographic separation was achieved by coupling two UPLC silica columns (Waters Acquity BEH HILIC, 2.1 \times 150 mm,
143 1.7 μ m) and a 2.1 \times 5 mm pre-column as in Hopmans et al. (2016), but with the following chromatographic modifications:
144 Mobile phases A and B consisted of *n*-hexane: chloroform (99:1, v/v) and *n*-hexane: 2-propanol: chloroform (89:10:1, v/v/v),
145 respectively. The flow rate was set to 0.4 ml/min and the columns heated to 50° C, resulting in a maximum backpressure of
146 425 bar. Sample aliquots of 20 μ l were injected with isocratic elution for 20 minutes using 86% A and 14% B, followed by a
147 gradient to 30% A and 70% B within the next 20 min. After this, the mobile phase was set to 100% B and the column rinsed
148 for 13 min, followed by 7 min re-equilibration time with 86% A and 14% B before the next sample analysis. The total run time
149 was 60 min.

150 IsoGDGTs were detected using positive ion APCI-MS and selective ion monitoring (SIM) of (M + H)⁺ ions (Schouten et
151 al., 2007) with the following settings: nebulizer pressure 50 psi, vaporizer and drying gas temperature 350° C, drying gas flow
152 5 L/min. The capillary voltage was 4 kV and the corona current +5 μ A. The detector was set for the following SIM ions: *m/z*
153 744 (C₄₆ standard), *m/z* 1302.3 (GDGT-0), *m/z* 1300.3 (GDGT-1), *m/z* 1298.3 (GDGT-2), *m/z* 1296.3 (GDGT-3), *m/z* 1292.3
154 (Crenarchaeol and Cren' isomer). The resulting scan/dwell time was 66 ms.

155 **4 Results and Discussion**

156 Our samples are located on a meridional transect along the Chilean margin extending into the DP, with changing environmental
157 conditions, in particular for SSTs, nutrients supply, salinity and current regimes. The U^K₃₇ values range from 0.07 (PS97/079)
158 to 0.38 (PS97/132), with minimum values in the southernmost region and increasing values to the north. All indices from

159 alkenones and isoGDGTs are listed in **Table A2**. In **Chapter 4.1** and **4.2**, we compare the two most widely used calibrations
160 for alkenones in this region: the subpolar and polar SO Sikes97 calibration, as well as the Müller98 calibration hereafter.

161 **4.1 Alkenone-based Sea Surface Temperatures**

162 Alkenone-based SSTs calculated with Müller98 range from $\sim 10^{\circ}\text{C}$ in the northernmost locations of our study area to $\sim 1^{\circ}\text{C}$
163 in the southern part of the Drake Passage, south of the PF (**Figure 2A, B**). SST estimates based on Sikes97 instead range from
164 $\sim 12.5^{\circ}\text{C}$ in the northernmost locations to $\sim 4^{\circ}\text{C}$ in the Drake Passage (**Figure 2C, D**). Most values fit closely to the Müller98
165 calibration line of both, annual mean and summer SSTs, but show an offset to the Sikes97 calibration line (**Figure 3**). Although
166 Sikes97 was specifically adapted to the subpolar and polar SO, it generally overestimates modern SSTs in this study area, both
167 for annual mean and summer (**Figure 2** and **Figure 3**). Our samples for the SE Pacific fit well to Müller98, but not to Sikes97
168 (**Figure 2** and **Figure 3**). Because of the latter's overestimation of modern temperatures, we hereafter chose to solely use the
169 Müller98 calibration.

170 **4.2 Influence of seasonality on alkenone temperature reconstruction**

171 **4.2.1 Seasonal signal along the Chilean Margin**

172 Our alkenone-based SSTs fits WOA05-derived annual mean and summer temperatures and show only a small seasonal effect
173 towards warmer SSTs. This observation is also in line with previous data from the Northern – Central Chilean Margin, which
174 yields a slight seasonal effect south of 50°S (Prahl et al., 2006; Prahl et al., 2010). Also, a previous study from the Chilean
175 fjord region confirms SST signals being only slightly shifted towards summer in the southern Chilean fjord region (**Figure 4**;
176 Caniupán et al., 2014). Along the Chilean continental margin, this seasonal summer effect even further decreases southward
177 to only $\sim 1^{\circ}\text{C}$ (i.e., summer SSTs vs. annual mean) between $50 - 57^{\circ}\text{S}$, based on WOA05-derived SSTs (**Figure 4**; blue and
178 yellow cross). This deviation of 1°C , at least north of the SAF, is within the generally accepted error range for alkenone-
179 derived paleo-SSTs of $\pm 1.5^{\circ}\text{C}$ (Müller et al., 1998), so that seasonality here appears to be negligible. Only further south in the
180 Drake Passage, deviations of our reconstructed summer temperatures from the annual mean increase to about 2°C , which are
181 likewise reflected in WOA05-based SSTs (**Figure 4**). Model results show a similar trend, with a small deviation from the
182 annual mean of up to 2.5°C at higher latitudes as well (Conte et al., 2006). Such an increasing poleward seasonality is not
183 unusual due to a temporal shift of the alkenone production towards summer (e.g., Volkman, 2000). Another effect that could
184 be involved in the increased seasonality is the reduction in the diversity and quantity of coccolithophores through the frontal
185 system of the ACC (e.g., Saavedra-Pellitero et al., 2014; Vollmar et al., 2022; Saavedra-Pellitero et al., 2019). The
186 coccolithophore assemblages between the PF and the SAF show a significantly reduced diversity compared to north of the
187 SAF. South of the PF, coccolithophorids occur only sporadically and show a reduced diversity (Saavedra-Pellitero et al., 2014).
188 In this region, we are nearing the lower temperature end and thus ecological boundary conditions for coccolithophores. So,

189 alkenone production could be biased towards warmer years within the inevitably large time period of several hundreds of years
190 that is comprised in the uppermost centimeter of surface sediment.

191 Not all data can be described by the poleward increase in the seasonal influence, since at two locations along the Chilean
192 margin an annual mean temperature is reflected instead (**Figure 4**; red circles). The first region is located between $\sim 54 - 58^\circ$ S
193 near the Strait of Magellan, where Atlantic waters mix with Pacific waters. The second region encompasses samples in the DP
194 located close to the PF. The PF marks the temperature boundary of the cold Antarctic surface water, which is subducted at the
195 PF and transported northwards (Orsi et al., 1995 - and references therein). This vertical water mass structure likely suppresses
196 potential seasonal effects by providing homogenous temperatures throughout the annual cycle, due to a reduce opportunity to
197 build up a warm summer surface layer.

198 This weakly expressed seasonality in our results, which remains mostly within the error range of Müller98, is in stark
199 contrast to results from other regions, notably the subarctic North Pacific. There, several studies showed a more consistent
200 seasonal shift towards summer and autumn SSTs of $4 - 6^\circ$ C north of the subarctic front, while locations south of the subarctic
201 front reflect an annual mean (Max et al., 2020; Méheust et al., 2013; Prahel et al., 2010). The subarctic front in the North Pacific
202 acts as a natural boundary, creating a highly stratified subarctic surface ocean with a permanent halocline and to pronounced
203 seasonal summer warming within strongly stratified surface waters. In contrast, the transition in the South Pacific from
204 subtropical to polar regions is characterized by a lower salinity gradient and stratification, leading to a less pronounced SAF.
205 The year-round deep mixing within the ACC prevents the formation of a prominent warm water layer during the summer.
206 Thus, subantarctic SSTs would be expected to show less seasonal influence on their SST signal.

207 **4.2.2 Regional synthesis of seasonality patterns across the South Pacific**

208 We compared the samples from our relatively small study region with published data from the South Pacific Gyre, the Central
209 South Pacific, the New Zealand Margin (Jaeschke et al., 2017) and the Northern – Central Chilean Margin (Prahel et al., 2006;
210 Prahel et al., 2010) based on the Müller98 and Sikes97 calibrations (**Figure 5**). We also calculated the residual temperatures by
211 subtracting the modern WOA05 temperatures at 10 m water depth from our calculated temperatures, shown in combination
212 with $U^{K'}_{37}$ against SSTs (**Figure 5**). The Central South Pacific and New Zealand Margin samples of Jaeschke et al. (2017)
213 spread over a wide area with different conditions. Taking into account a seasonal effect towards summer SSTs, only few
214 samples of this extended data set match with the Sikes97 calibration (**Figure 5A, B**; Jaeschke et al., 2017). This is partly in
215 contrast to Jaeschke et al. (2017) who concluded that alkenone-derived SSTs in general best reflect the austral summer months
216 when using Sikes97 calibration. The Müller98 calibration is applicable in the entire extended study area when compared with
217 both, annual mean and summer SSTs, reaffirming our decision to use Müller98 for further analyses.

218 The SCM and the Drake Passage samples are generally warmer by $\sim 1.5^\circ$ C than the samples from the Central South Pacific
219 region (**Figure 6**). The Central South Pacific samples represent a best fit to annual mean, in contrast to the SCM and DP
220 samples, which have a slight, but mostly negligible, seasonal shift toward summer SSTs (**Figure 6**). The most likely reason
221 for this bias to summer SSTs in the SE-Pacific could be a higher nutrient availability during the summer months due to the

222 close proximity of the SE Pacific samples to South America. High nutrient availability could lead to a potentially changing
223 competition between different primary producers, e.g., high silica input favors a diatom bloom, which changes when silica is
224 depleted (e.g., Durak et al., 2016; Smith et al., 2017; Tyrrell and Merico, 2004). In this region, nutrient input is expected to be
225 highest during austral summer months, when the high precipitation rates of 3,000 – 10,000 mm/yr in South Patagonia reach
226 their maximum (e.g., Garreaud et al., 2013; Lamy et al., 2010; Schneider et al., 2003). The increased precipitation during
227 summer months results in an increased freshwater runoff (e.g., Dávila et al., 2002), accompanied by increased supply of
228 continent-derived nutrients to hemipelagic and DP waters and a more stable seasonal thermocline (Toyos et al., 2022), which
229 would both favor a seasonal coccolithophore bloom.

230 The area off New Zealand correlates well with samples off the Northern – Central Chilean Margin north of ~45° S and
231 corresponds to the annual mean (**Figure 6**). In contrast, the South Pacific Gyre samples reflect a summer to autumn signal
232 (**Figure 6**; Jaeschke et al., 2017). The South Pacific Gyre is characterized by extremely low nutrient content and accordingly
233 low primary production (D'hondt et al., 2009). Reasons for the low nutrient content here are the distance from potential
234 continental inputs, and a relatively deep thermocline setting, which reduces upwelling and nutrient advection (D'hondt et al.,
235 2009; Lamy et al., 2014). This is reflected by low alkenones, *n*-alkanes and branched (br)GDGTs concentrations (Jaeschke et
236 al., 2017). These factors likely lead to a seasonal bias if e.g., dust transport and macronutrient supply are increased in late
237 spring to summer and relatively quickly exhausted.

238 4.3 GDGT – based (sub)surface temperatures

239 Similar to U^{K}_{37} values, isoGDGT-derived indices TEX^{H}_{86} and TEX^{L}_{86} increase along our transect from south to north. The
240 values range from –0.48 to –0.61 (PS97/079) and from –0.39 to –0.53 (PS97/131) for TEX^{H}_{86} and TEX^{L}_{86} , respectively (cf.
241 **Table A2**). In contrast to Coccolithophorids, *Thaumarchaeota* live at greater water depths (e.g., Karner et al., 2001) and occur
242 also in the polar regions (e.g., Massana et al., 1998; Murray et al., 1998), which complicates the choice of an adequate
243 temperature calibration, since reference data and sample sites for both characteristics remain scarce. For the isoGDGTs, we
244 use six calibrations in total for both indices: the surface calibrations $SST^{H}Kim$, $SST^{H}Kaiser$ and $SST^{L}Kim$, as well as the
245 subsurface calibrations $Tsub^{H}Kim$, $Tsub^{H}Kaiser$ and $Tsub^{L}Kim$ (**Table A1**).

246 Surface and subsurface ranges for isoGDGTs are following the definition of Kaiser et al. (2015), Kim et al. (2012b) and
247 Kim et al. (2012a), with a mean of 0 – 50 m water depth and 0 – 200 m water depth, respectively. We therefore used the
248 WOA05-derived temperatures of depths from 10 m and 125 m for surface and subsurface, as they roughly correspond to the
249 average values (**Figure 7**). Based on the surface calibrations, the temperatures range from ~11.5° C to 5° C for $SST^{H}Kim$,
250 from ~9.5° C to 4° C for $SST^{H}Kaiser$, and from ~13° C to 6° C for $SST^{L}Kim$. With the subsurface calibrations, the
251 temperatures range from ~9° C to 4° C for $Tsub^{H}Kim$, ~9° C to 5° C for $Tsub^{H}Kaiser$, and from ~10° C to 5° C for $Tsub^{L}Kim$
252 (**Figure 7**).

253 The locations north of the SAF fit best to the modern WOA05-derived SSTs with the $SST^{H}Kaiser$ calibration (**Figure 7B**)
254 and appear to extend the surface regression line along the 5 – 10° C temperature range (**Figure 8A**). On average, the modern

255 temperatures are overestimated by $\sim 1.3^\circ\text{C}$, which means they are no longer within the $\pm 0.8^\circ\text{C}$ standard error determined by
256 Kaiser et al. (2015) for the surface calibration. In the subsurface, the $T_{\text{sub}}^{\text{HKim}}$ and $T_{\text{sub}}^{\text{HKaiser}}$ calibrations equally fit the
257 modern WOA05-derived T_{sub} (**Figure 7D, E**), but the samples tend to fit better with the calibration line of $T_{\text{sub}}^{\text{HKim}}$ (**Figure**
258 **8B**). On average, the modern WOA05-derived T_{sub} are overestimated here by $\sim 1.6^\circ\text{C}$. Thus, the calculated temperatures are
259 within the of $\pm 2.2^\circ\text{C}$ error range given by Kim et al. (2012a), but not within the $\pm 0.6^\circ\text{C}$ given by Kaiser et al. (2015) for the
260 subsurface calibration. The samples from the DP instead do not fit to any calibration and overestimate modern WOA05-derived
261 SSTs or T_{sub} in all calibrations, leading us to compare our results to other previously published data (see **Chapter 4.5; Figure**
262 **7 and Figure 8**).

263 Apart from absolute temperature values, the slope of various calibrations allows to calculate relative temperature changes
264 through time in marine sediment cores. Hence, the slope of the used temperature calibration in an area should adequately
265 resemble the magnitude of relative temperature changes (e.g., between glacial and interglacial periods) to provide correct ΔT ,
266 which is e.g., often used in modelling studies (Burke et al., 2018), even if absolute temperature is offset. To determine which
267 calibration best captures relative temperature changes in our study region, we compared our samples with published data from
268 the Central South Pacific and New Zealand Margin (Ho et al., 2014; Jaeschke et al., 2017), in addition to the Northern – Central
269 Chilean Margin (Kaiser et al., 2015) dataset (**Figure 9**). In **Figure 9A – D** we show in red the regressions of all sites located
270 north of the SAF (called “local regression” hereafter) in comparison to the published six different SST and T_{sub} calibrations
271 of Kim et al. (2010, 2012a and b), and Kaiser et al. (2015). In addition, we show the residuals in **Figure 9E, F** to illustrate
272 which data are within the error range of the respective calibrations. For this purpose, the mean WOA05 values of 0 – 50 m and
273 0 – 200 m of the annual mean were subtracted from the respective temperature calibration.

274 The slope of the SST^{HKim} calibration shows a difference of ~ 3.2 to our local regression (**Figure 9A**), and yields best the
275 relative temperature change across the region north of the SAF, although it generally yields the highest residuals (**Figure 9E**).
276 The $T_{\text{sub}}^{\text{HKim}}$ calibration, with a difference of ~ 3.9 between the two slopes (**Figure 9C**), captures the relative temperature
277 changes as well. The latter corresponds to a temperature change ($\text{TEX}^{\text{H}_{86}}$: -0.2 to -0.3) of 5.5°C with $T_{\text{sub}}^{\text{HKim}}$ and 5.1°C
278 with our local regression. In contrast to SST^{HKim} , the residuals are smaller and within the reported error range of $\pm 2.2^\circ\text{C}$
279 (Kim et al., 2012a) for most samples north of the SAF (**Figure 9F**). Again, the central South Pacific samples located south of
280 the SAF significantly overestimate local SSTs or T_{sub} with annual residuals of $\sim 8.4^\circ\text{C}$ (SST^{HKim}), $\sim 6.6^\circ\text{C}$ ($\text{SST}^{\text{HKaiser}}$),
281 $\sim 8.1^\circ\text{C}$ (SST^{LKim}), $\sim 6.4^\circ\text{C}$ ($T_{\text{sub}}^{\text{HKim}}$), $\sim 6.9^\circ\text{C}$ ($T_{\text{sub}}^{\text{HKaiser}}$) and $\sim 6.7^\circ\text{C}$ ($T_{\text{sub}}^{\text{LKim}}$).

282 Thus, our combined sample set north of the SAF fits the $T_{\text{sub}}^{\text{HKim}}$ calibration best, while the samples south of the SAF
283 do not match the commonly used calibrations, including the two calibrations based on $\text{TEX}^{\text{L}_{86}}$ for (sub)polar regions (Kim et
284 al., 2012b; Kim et al., 2010).

285 4.4 Influence of habitat depth and terrestrial input on *Thaumarchaeota*-derived temperatures

286 Habitat depth preferences for *Thaumarchaeota* and their response to seasonality (e.g., Schouten et al., 2013a) may influence
287 the $\text{TEX}^{\text{H}_{86}}$ -derived temperature signals. Since *Thaumarchaeota* are distributed throughout the entire water column, the

288 decision to choose an optimal calibration is closely linked to an initial assumption about the water depth from which the signal
289 originates (Karner et al., 2001). Hence, we applied the ratio of GDGT-2 to GDGT-3 (GDGT [2]/[3]) to locate the water depth
290 of the temperature signal, since subsurface dwelling *Thaumarchaeota* preferentially yield GDGT-2 over the GDGT-3 (Kim et
291 al., 2015; Taylor et al., 2013).

292 In the global ocean the distribution of *Thaumarchaeota* appears to vary within the water column and shows an increasing
293 GDGT [2]/[3]-ratio with increasing depth (Dong et al., 2019; Hernández-Sánchez et al., 2014; Kim et al., 2015; Kim et al.,
294 2016; Schouten et al., 2012; Taylor et al., 2013). Water column samples in the Arabian Sea and along the Portuguese margin
295 show a GDGT [2]/[3]-ratio between <3.3 in the upper 50 m and 4.0 – 21.5 at >200 m water depth (Dong et al., 2019; Kim et
296 al., 2016; Schouten et al., 2012). In the South China Sea, the GDGT [2]/[3]-ratio yields <3.5 at <100 m water depth and
297 5.9 – 8.6 at water depth >300 m (Dong et al., 2019). In the Southeast Atlantic, the GDGT [2]/[3]-ratio of between 0 – 50 m
298 water depth is 1.9 – 3.4, 4.1 – 12.8 between 50 – 200 m water depth and 13 – 50 in water depth >200 m (Hernández-Sánchez
299 et al., 2014). Thus, increasing GDGT [2]/[3]-ratios may not be strictly coupled to water depths across the world ocean. The
300 GDGT [2]/[3]-ratio in the surface area seems similar in all regions with ~3.5, but subsurface values differ considerably. In the
301 Southern Atlantic, the GDGT [2]/[3]-ratio increases to up to 12.8 within 50 – 200 m water depth, whereas at the Portuguese
302 margin, the Arabian and the South China Sea, the GDGT [2]/[3]-ratio increases up to ~5.0, with oxygen content or nutrients
303 being the most likely reason for such non-linearities (e.g., Basse et al., 2014; Villanueva et al., 2015).

304 The GDGT [2]/[3]-ratios in our extended study area vary between ~3 – 25. Values <5 (n = 7), indicating a surface signal,
305 are found only occasionally off New Zealand and along the Chilean Margin. The majority of samples would correspond to a
306 subsurface signal with a GDGT [2]/[3]-ratio >5, confirming our calibration choice (T_{sub}^{HKim}) for the South Pacific. Studies
307 from the Humboldt Current system, the Antarctic Peninsula and the North Pacific Gyre confirm this assumption and indicate
308 a subsurface rather than a surface signal (Kalanetra et al., 2009; Karner et al., 2001; Massana et al., 1998; Quiñones et al.,
309 2009). Here, we will distinguish between shallower subsurface (0 – 200 m water depth) and deep subsurface (>200 m water
310 depth), to quantify the influence of deep subsurface-dwelling *Thaumarchaeota* to the GDGT distribution in the sediment. In
311 general, it is assumed that a deep subsurface water influence is comparatively small, since *Thaumarchaeota* can be most
312 effectively grazed, packed into fecal pellets, and transported to the seafloor within the photic zone (Wuchter et al., 2005).
313 Nevertheless, variations in the GDGT [2]/[3]-ratio across the entire study area can provide information about regions that may
314 be subject to a greater influence of deep subsurface dwelling *Thaumarchaeota*. Our South Pacific locations yield differences
315 in GDGT [2]/[3]-ratio according to three principally differing boundary or forcing conditions: A hemipelagic continental
316 margin setting, a deep thermocline oligotrophic gyre setting, and a SO frontal setting (**Figure 10**).

317 In the overall study area, our results suggest that isoGDGTs record shallower subsurface temperatures rather than surface
318 temperatures. Samples along continental slopes tend to be less influenced by deep subsurface-dwelling *Thaumarchaeota*, while
319 samples from the pelagic regions show a greater influence by deep subsurface-dwelling *Thaumarchaeota*. Samples along the
320 Chilean Margin yield a mean GDGT [2]/[3]-ratio of ~6.2 to ~6.9, reflecting a transition between surface and shallow subsurface
321 habitats. This is in line with Northern – Central Chilean Margin data, which show a positive correlation with both SSTs and

322 Tsub (Kaiser et al., 2015). The amount of deep subsurface-dwelling *Thaumarchaeota* increase with increasing distance from
323 land, as shown by samples from the SW Pacific close to New Zealand. The GDGT [2]/[3]-ratios increase, in line with Taylor
324 et al. (2013), from ~3.1 at ~600 m water depth to ~9.8 at >3000 m water depth to ~12.9 at >4000 m water depth (**Figure 10**).
325 The highest influence of deep-dwelling *Thaumarchaeota* occurs in the South Pacific Gyre and in the eastern South Pacific,
326 averaging a GDGT [2]/[3]-ratio of ~11.5 and indicating a potentially larger contribution of deep subsurface-dwelling
327 *Thaumarchaeota* communities in the sediment, but no significant temperature deviations can be detected for the region north
328 of the SAF (**Figure 9**). This suggests either that the influence of the deep subsurface-dwelling *Thaumarchaeota* on the
329 temperature signal is smaller than previously thought, or that the distribution of the GDGT [2]/[3]-ratio in the subsurface in
330 this region differs from that in the central South Pacific or continental margins.

331 Besides contributions from deeper living *Thaumarchaeota*, the GDGT [2]/[3]-ratio can also be influenced by isoGDGTs
332 derived from terrestrial soils and peats, where the amount of the GDGT-3 is increased compared to the marine milieu (Weijers
333 et al., 2006). This would result in GDGT [2]/[3]-ratio decreases with increasing terrestrial input, i.e., in the opposite direction
334 of the influence of deeper living *Thaumarchaeota*. Therefore, we showed the GDGT [2]/[3]-ratios on a map with monthly
335 average dust depositions (**Figure 12**) and found high GDGT [2]/[3]-ratios in areas with very little dust accumulation and lower
336 GDGT [2]/[3]-ratios with higher dust accumulation, especially during march. This could explain the discrepancy between
337 eastern and western pelagic South Pacific at a first glance and fit also to the low GDGT [2]/[3]-ratios along continental margins.
338 To detect such distortions of terrigenous isoGDGTs on the GDGT [2]/[3]-ratio and therefore the TEX-based indices, the
339 branched vs isoprenoid tetraether (BIT; should be <0.3) index was developed, where the brGDGTs occurring predominantly
340 in terrestrial soils are related to the Crenarchaeol (Hopmans et al., 2004). The BIT is low (≤ 0.1) in this region, indicating no
341 significant influence from land (Jaeschke et al., 2017; Kaiser et al., 2015). The visually good correlation between the GDGT
342 [2]/[3]-ratios and the dust distribution indicates that future studies could potentially address more systematically underlying
343 causes of these co-variations, at least in regions with low sedimentation rates but likely high eolian transport. Generally,
344 however, isoGDGT-derived temperatures of samples north of the SAF fit quite well with Tsub^HKim, so that both potential
345 influences, deeper-dwelling *Thaumarchaeota* as well as terrigenous input seems to be negligible.

346 **4.5 Towards an alternative southern hemisphere (sub)-polar calibration for isoGDGT-based temperatures**

347 IsoGDGTs south of the SAF appear to have a lower sensitivity to temperature, which is in line with previous results,
348 showing a large scatter of the TEX₈₆ – SST relationship in the polar regions (e.g., Kim et al., 2010; Fietz et al., 2020 and
349 references therein). One reason given for the larger scatter may be a calibration based on satellite-assigned SSTs, which in
350 polar regions yields values below the freezing point of seawater (Pearson and Ingalls, 2013). Consequently, a larger scatter of
351 polar samples leads to a larger error of estimate in the related calibrations and would explain the occurrence of highest residuals
352 with SST^HKim and SST^LKim in our study area in both north and south of the SAF (**Figure 7, 9**), i.e., where calibrations are
353 based on satellite-assigned SSTs. However, our data does not show an increased scatter of values south of the SAF. Instead,

354 they show a different TEX^{H}_{86} (TEX^{L}_{86}) – water temperature relationship, resulting in a lower slope of the calibration line
355 (**Figure 9**).

356 We suspect that the SAF acts as a natural boundary, leading to differential responses within the *Thaumarchaeota*
357 communities and their respective isoGDGTs to changing environmental parameters such as pH (Elling et al., 2015) or oxygen
358 availability (Qin et al., 2015). Another reason for this pattern could be the increased occurrence of OH-isoGDGTs in polar
359 regions. OH-isoGDGTs are present in lower amounts in the sediment than the isoGDGTs used in TEX^{H}_{86} and TEX^{L}_{86} , but are
360 most abundant in higher latitudes (Fietz et al., 2013; Huguet et al., 2013; Liu et al., 2020). This increased occurrence of OH-
361 isoGDGTs could indicate an adaptation to cold temperatures to maintain membrane fluidity. This could simultaneously affect
362 the relationship of TEX-based indices to temperature, requiring a separate calibration for high latitudes. OH-isoGDGTs also
363 show a stronger correlation with water temperature than isoGDGTs in both the Arctic (Fietz et al., 2013) and close to Antarctica
364 (Liu et al., 2020), so another OH-isoGDGT-based index RI-OH' (= $[OH-GDGT-1]+2*[OH-GDGT-2]/[OH-GDGT-0]+[OH-$
365 $GDGT-1]+[OH-GDGT-2]$; $SST = (RI-OH' - 0.1)/0.0382$) has been proposed for polar regions (Lü et al., 2015). Moreover, OH-
366 isoGDGTs were often not measured in legacy samples reported in early studies. Based on this, Fietz et al. (2020) recommended
367 a multi-proxy approach for the polar regions, which includes both isoGDGTs and OH-isoGDGTs. However, isoGDGTs were
368 more commonly used and OH-isoGDGTs may not be available for some data sets. A good example are the data sets (e.g.)
369 Tsub^LKim with $n = 396$ (Kim et al., 2012b) and RI-OH'-based surface calibration with $n = 107$ (Lü et al., 2015), which are
370 designated for the same temperature range $<15^{\circ}C$. A working TEX-based calibration specifically developed for the SO is
371 therefore appropriate and may also be useful for further research on the functionality (OH)-isoGDGTs. Therefore, we here
372 take an initial step and propose a modified TEX-based cold temperature calibration for the southern hemisphere (sub)polar
373 region. We will then test the new calibration by (1) re-estimating the temperatures of a published sediment core and (2)
374 comparing the SSTs and Tsub determined with the new calibration to RI-OH'-based SSTs.

375 This suggested calibration includes samples south of the SAF in the SO, and is extended by the data sets of Kim et al.
376 (2010) and Lamping et al. (2021) with a total of $n = 137$ samples. Changes in TEX^{H}_{86} or general TEX_{86} indices below $5^{\circ}C$
377 water temperature (according to SSTs south of the SAF in the Southern Ocean) are less pronounced than above $5^{\circ}C$, because
378 of a weaker correlation of the isomer Cren' to water temperatures. Thus, it is excluded in the TEX^{L}_{86} – index as proposed by
379 earlier studies (Kim et al., 2010). This is in line with our results, where all TEX^{L}_{86} calibrations show a stronger correlation
380 than those based on TEX^{H}_{86} (cf. determination coefficient R^2 ; **Figure 11**). The maximum R^2 value of 0.7 (TEX^{L}_{86} , subsurface)
381 is only slightly lower than previously published values (>0.8 , cf.; **Table A1**), which is to be somewhat expected, because the
382 scatter of both TEX^{H}_{86} and TEX^{L}_{86} indices below $5^{\circ}C$ seems to be generally larger (Ho et al., 2014).

383 Based on our results, we propose a new TEX^{L}_{86} – based annual mean, subsurface (0 – 200 m) and surface (0 – 50 m)
384 calibration for the Southern Ocean's polar and subpolar regions:

385

$$386 \quad T_{sub} = 14.38 * TEX^{L}_{86} + 8.93, \quad (1)$$

$$387 \text{ SST} = 10.71 * \text{TEX}_{86}^L + 6.64, \quad (2)$$

388

389 The standard error of $\pm 0.6^\circ \text{C}$ ($\pm 0.5^\circ \text{C}$) for our subsurface (surface) calibration is lower than the standard error from the
390 previous subsurface (surface) calibration Tsub^LKim (SST^LKim) with $\pm 2.8^\circ \text{C}$ ($\pm 4^\circ \text{C}$), which is probably due to the latter's
391 lower data density. With this new calibration, just 44 (40) of the 137 samples lie outside this error range. Another major
392 difference between our calibration and Tsub^LKim (SST^LKim) is the slope of the regression line being much flatter here at 14.4
393 (10.7) than the slope of the calibration Tsub^LKim (SST^LKim) with 50.8 (67.5) (**Figure 9**). This leads to a generally smaller
394 temperature increase with an increasing TEX_{86}^L index. An increase of TEX_{86}^L from -0.6 to -0.5 e.g., corresponds to a
395 temperature change of 1.4°C in our subsurface calibration and of 5.1°C in Tsub^LKim.

396 (1) Using our new calibration, we compare recalculated results with the previously used subsurface TEX_{86}^L calibration
397 Tsub^LKim (**Figure 13**) on core MD03-2601 ($66^\circ 03.07' \text{ S}$, $138^\circ 33.43' \text{ E}$; Kim et al., 2012b) from the eastern Indian sector of
398 the SO covering the Holocene, where the authors acknowledged that a temperature offset existed, but within the specified
399 calibration error range of $\pm 2.8^\circ \text{C}$. Temperatures based on our subsurface calibration are on average $\sim 2.5^\circ \text{C}$ colder than the
400 ones based on the previously used subsurface calibration Tsub^LKim. With our new calibration, temperatures remain relatively
401 constant at -0.8°C , and at 1.5°C with the subsurface calibration Tsub^LKim between 4.8 – 3.1 ka BP. Modern temperatures
402 near the core site agree well with core top results from our new calibration with -0.7°C (65.5° S , 138.5° E ; Locarnini et al.,
403 2006) vs. -0.8°C (our reconstruction) for the subsurface layer. The recalculated temperature increases, associated with warmer
404 nutrient-rich modified Circumpolar Deep-Water intrusions, show an attenuated amplitude with the new calibration
405 (**Figure 13**). The amplitude based on our new calibration is 1.2°C around 1.7 ka BP, whereas it is 4.2°C with the original
406 subsurface calibration Tsub^LKim and therefore better fits to the expected temperatures.

407 (2) While we do not have OH-isoGDGTs for the Kim et al. (2010), Jaeschke et al. (2017) and Ho et al. (2012) datasets, we
408 calculated SSTs based on the RI-OH' index and compared them to SSTs and Tsub based on our calibrations for all samples
409 south of the SAF for which OH-isoGDGTs are available (Drake Passage, Antarctic Peninsula, Weddell Sea and Amundsen
410 Sea). The results of all three calibrations (TEX_{86}^L -based SST and Tsub; RI-OH'-based SST) fit (**Figure 14**), with a temperature
411 discrepancy of $\pm 1^\circ \text{C}$ from each other. One exception here is the Drake Passage, where the RI-OH'-based SSTs show residuals
412 of $> 2^\circ \text{C}$. Considering the standard error of $\pm 6^\circ \text{C}$ (Lü et al., 2015), all RI-OH'-based SSTs are within this error range. The
413 upper ocean temperatures in the Drake Passage are the only ones in this area above zero, which may explain the larger residuals
414 of the RI-OH'-based SSTs. It is possible that similar to the subsurface calibration of Kim et al. (2012b), the relative temperature
415 change is not correctly captured due to a too steep regression line for samples south of the SAF. The calibration of Lü et al.
416 (2015) includes only a few samples from higher latitudes, most of them from the Arctic, and samples in the temperature range
417 between $1 - 3^\circ \text{C}$ are almost absent. A RI-OH'-based calibration for samples south of the SAF could increase the sensitivity
418 of the proxy and decrease the standard error, similar to the TEX_{86}^L -index demonstrated here. This is in contrast to the good
419 agreement of the remaining samples, both with our TEX -based temperature reconstructions and with the WOA05-derived

420 temperatures. A calibration based on $\text{TEX}^{\text{L}}_{86}$ developed specifically for the SO yields comparable results to a calibration based
421 on OH-isoGDGTs. We agree with Fietz et al. (2020) to determine both indices, if possible, as this is a good way to check the
422 consistency of temperature reconstructions.

423

424 **5 Conclusion**

425 In this study, we provide a qualitative evaluation of the most common temperature calibrations for alkenones and
426 isoGDGTs in the South Pacific and potential environmental influencing factors. For alkenone-derived SSTs, our results
427 provide a best fit with the global core-top calibration of Müller et al. (1998). On a regional scale, the Southern Chilean Margin
428 and the Drake Passage show a small seasonal effect of $\sim 1^\circ\text{C}$ towards warmer SSTs south of $\sim 50^\circ\text{S}$, albeit well within the
429 $\pm 1.5^\circ\text{C}$ standard error for alkenone derived SSTs (Müller et al., 1998). Excluding local influences, the seasonal effect in the
430 DP is slightly higher at about $\sim 2^\circ\text{C}$ and no longer within the error range of calibration by Müller et al. (1998). In contrast, the
431 samples from the Central Southern Pacific Ocean show no clear seasonal trend. Causes for this difference between the two
432 areas are increased seasonal provision of nutrients, or more pronounced stratification at the sites proximal to continental runoff
433 along the Chilean margin during late summer time.

434 IsoGDGT-based temperatures show a more complex pattern, which necessitates choosing the temperature calibration
435 carefully, depending on the area. The optimal calibration for isoGDGT-based temperature reconstructions in the South Pacific
436 is the subsurface calibration T_{sub} (Kim et al., 2012a), for samples north of the Sub-Antarctic Front, in line with evidence from
437 compiled GDGT [2]/[3]-ratios, which indicate a subsurface of 0 to 200 m water depth, rather than surface habitat depth
438 throughout the study area. South of the Sub-Antarctic Front, all existing calibrations overestimate local WOA05-derived
439 temperatures. Furthermore, the GDGT [2]/[3]-ratios do also correlate with the average monthly dust deposition in the South
440 Pacific. A new calibration for subpolar and polar areas yields lower absolute subsurface temperatures, as well as lower relative
441 changes within the commonly accepted standard error range. The results of this new calibration fit well within the standard
442 error with OH-GDGT-derived temperatures.

443 For future work, we recommend to extend both the geographical area coverage in subpolar and polar regions and the sample
444 density. Furthermore, the influence of seasonality and habitat should be investigated to assess how strongly these factors affect
445 paleo-temperature reconstructions.

446 **Appendix A**

447 **Table A1: Common indices and their most important temperature calibrations for alkenones and isoGDGTs, with their**
448 **determination coefficients (R^2) and abbreviations used in this paper. U^{K}_{37} = Alkenone unsaturation index consisting of 37 carbon**
449 **atoms; TEX_{86} = Tetraether index consisting of 86 carbon atoms; $\text{TEX}^{\text{H}}_{86}$ = Tetraether index for water temperatures above 15°C ;**
450 **$\text{TEX}^{\text{L}}_{86}$ = Tetraether index for water temperatures below 15°C ; SST = Sea Surface Temperature; T_{sub} = Sea subsurface**
451 **temperatures (0 – 200 m water depth). Abbreviation: the here defined abbreviations will be used in the main text.**

	Equation	R ²	Abbreviation	References
1	$U_{37}^K = [C_{37:2}] / [C_{37:2}] + [C_{37:3}]$			Prahl and Wakeham (1987)
2	$SST = (U_{37}^K - 0.043) / 0.033$	0.994		Prahl and Wakeham (1987)
3	$SST = (U_{37}^K - 0.039) / 0.034$	0.994	Prahl88	Prahl et al. (1988)
4	$SST = (U_{37}^K - 0.044) / 0.033$	0.958	Müller98	Müller et al. (1998)
5	$SST = (U_{37}^K + 0.082) / 0.038$	0.921	Sikes97	Sikes et al. (1997)
6	$TEX_{86} = \frac{[2] + [3] + [Cren']}{[1] + [2] + [3] + [Cren']}$			Schouten et al. (2002)
7	$TEX_{86}^H = \log \frac{[2] + [3] + [Cren']}{[1] + [2] + [3] + [Cren']}$			Kim et al. (2010)
8	$TEX_{86}^L = \log \frac{[2]}{[1] + [2] + [3]}$			Kim et al. (2010)
9	$SST = 68.4 * TEX_{86}^H + 38.6$	0.87	SST ^H Kim	Kim et al. (2010)
10	$Tsub = 54.7 * TEX_{86}^H + 30.7$	0.84	Tsub ^H Kim	Kim et al. (2012a)
11	$SST = 59.6 * TEX_{86}^H + 33$	0.91	SST ^H Kaiser	Kaiser et al. (2015)
12	$Tsub = 32.1 * TEX_{86}^H + 21.5$	0.86	Tsub ^H Kaiser	Kaiser et al. (2015)
13	$SST = 67.5 * TEX_{86}^L + 46.9$	0.86	SST ^L Kim	Kim et al. (2010)
14	$Tsub = 50.8 * TEX_{86}^L + 36.1$	0.87	Tsub ^L Kim	Kim et al. (2012b)

453 Table A2: Surface sediment sample results of this study. $U^{K'_{37}}$ = Alkenone unsaturation index consisting of 37 carbon atoms; TEX_{86}
 454 = Tetraether index consisting of 86 carbon atoms; TEX_{86}^H = Tetraether index for water temperatures above 15° C; TEX_{86}^L =
 455 Tetraether index for water temperatures below 15° C.

	Station	Latitude	Longitude	Depth [m]	$U^{K'_{37}}$	TEX_{86}^H	TEX_{86}^L
	<i>Southern Chilean Margin</i>						
1	PS97/139-1	52° 26.56' S	75° 42.42' W	640	0.40	-0.40	-0.58
2	PS97/134-1	52° 40.97' S	75° 34.85' W	1075.1	0.36	-0.39	-0.54
3	PS97/132-2	52° 37.01' S	75° 35.14' W	843	0.38	-0.47	-0.60
4	PS97/131-1	52° 39.58' S	75° 33.97' W	1028.2	0.35	-0.39	-0.53
5	PS97/129-2	53° 19.28' S	75° 12.84' W	1879.4	0.34	-0.41	-0.54
6	PS97/128-1	53° 38.04' S	75° 32.71' W	2293.7	0.32	-0.42	-0.54
7	PS97/122-2	54° 5.85' S	74° 54.89' W	2560	0.31	-0.41	-0.53
8	PS97/114-1	54° 34.68' S	76° 38.85' W	3863	0.26	-0.41	-0.50
9	PS97/027-1	54° 23.05' S	74° 36.30' W	2349.2	0.28	-0.41	-0.53
10	PS97/024-2	54° 35.27' S	73° 57.30' W	1272.8	-	-	-
11	PS97/022-1	54° 42.03' S	73° 48.38' W	1615.1	0.27	-0.41	-0.55
12	PS97/021-1	55° 6.91' S	72° 40.09' W	1840.4	0.30	-0.41	-0.54
13	PS97/020-1	55° 30.80' S	71° 38.22' W	2104.3	0.27	-0.42	-0.54
14	PS97/015-2	55° 43.89' S	70° 53.55' W	1886.3	0.31	-0.42	-0.55
15	PS97/094-1	57° 0.17' S	70° 58.32' W	3993.4	0.31	-0.39	-0.52
16	PS97/093-3	57° 29.92' S	70° 16.57' W	3782.2	0.36	-0.42	-0.54
17	PS97/097-1	57° 3.27' S	67° 4.00' W	2318.6	0.30	-0.42	-0.53
18	PS97/096-1	56° 4.53' S	66° 8.96' W	1620.7	0.31	-0.44	-0.55
19	PS97/095-1	56° 14.68' S	66° 14.95' W	1652.1	0.25	-0.43	-0.55
	<i>Drake Passage Shackleton Fracture Zone</i>						
20	PS97/089-2	58° 13.60' S	62° 43.63' W	3431.9	0.18	-0.43	-0.56
21	PS97/086-2	58° 38.65' S	61° 23.82' W	2968.9	0.15	-0.45	-0.56

22	PS97/085-2	58° 21.28' S	62° 10.07' W	3090.7	0.16	-0.43	-0.55
23*	PS97/084-2	58° 52.14' S	60° 51.91' W	3617.4	0.10	-0.46	-0.58
24*	PS97/083-1	58° 59.65' S	60° 34.28' W	3756.3	0.12	-0.49	-0.60
25*	PS97/080-2	59° 40.49' S	59° 37.86' W	3112.7	0.12	-0.46	-0.56
26*	PS97/079-1	60° 8.55' S	58° 59.42' W	3539.3	0.07	-0.48	-0.61
<i>Drake Passage Phoenix Antarctic Ridge</i>							
27*	PS97/042-1	59° 50.62' S	66° 5.77' W	4172	0.12	-0.43	-0.54
28*	PS97/044-1	60° 36.80' S	66° 1.34' W	1202.8	-	-0.48	-0.57
29*	PS97/045-1	60° 34.27' S	66° 5.67' W	2292	0.14	-0.47	-0.55
30*	PS97/046-6	60° 59.74' S	65° 21.40' W	2802.7	0.13	-0.45	-0.56
31*	PS97/048-1	61° 26.40' S	64° 53.27' W	3455.2	0.14	-0.42	-0.55
32*	PS97/049-2	61° 40.28' S	64° 57.74' W	3752.2	0.14	-0.47	-0.58
33*	PS97/052-3	62° 29.93' S	64° 17.63' W	2889.8	-	-0.46	-0.60

456 * isoGDGTs Lamping et al. (2021); Alkenone *this study*

457

458 **Data availability.** All locations and the three main indices of the new 33 samples of this study are available in **Table A2**.

459

460 **Author contributions.** The study was conceived by JRH and LL-J; MEV, JRH, JH and NR contributed with analytical tools;
 461 JRH, LL-J, JK, AJ analyzed data; JRH drafted the paper and figures; LL-J supervised the study. All authors contributed to the
 462 interpretation and discussion of the results as well as commented on, or contributed to the draft and final version of the
 463 manuscript.

464

465 **Acknowledgements.** We thank master and crew of R/V Polarstern, as well as the science party for their professional support
 466 on expedition PS97 “Paleo-Drake”. We thank Sophie Ehrhardt for providing unpublished alkenone data. We thank the
 467 technicians Walter Luttmner and Denise Dickstall for their support in the laboratory. We acknowledge funding through the
 468 AWI institutional research programs “PACES-II” and “Changing Earth – Sustaining our Future”, as well as through the
 469 REKLIM initiative. We acknowledge the use of imagery from the NASA Worldview application
 470 (<https://worldview.earthdata.nasa.gov/>), part of the NASA Earth Observing System Data and Information System (EOSDIS).
 471 We thank the two anonymous reviewers and the editor for their constructive, detailed, and very helpful comments, which
 472 allowed us to improve our work significantly.

473

474

475 **Financial support.** This research has been supported by the AWI institutional research programs “PACES-II” and “Changing
476 Earth – Sustaining our Future”, as well as through the REKLIM initiative.

477

478 **Competing Interests.** The authors declare no conflict of interest.

479

480 **References**

- 481 Basse, A., Zhu, C., Versteegh, G. J. M., Fischer, G., Hinrichs, K. U., and Mollenhauer, G.: Distribution of intact and core tetraether lipids in
482 water column profiles of suspended particulate matter off Cape Blanc, NW Africa, *Organic Geochemistry*, 72, 1-13,
483 10.1016/j.orggeochem.2014.04.007, 2014.
- 484 Baumann, K.-H., Andrulleit, H., Böckel, B., Geisen, M., and Kinkel, H.: The significance of extant coccolithophores as indicators of ocean
485 water masses, surface water temperature, and palaeoproductivity: a review, *Paläontologische Zeitschrift*, 79, 93-112,
486 10.1007/bf03021756, 2005.
- 487 Belt, S. T., Brown, T. A., Ampel, L., Cabedo-Sanz, P., Fahl, K., Kocis, J. J., Massé, G., Navarro-Rodriguez, A., Ruan, J., and Xu, Y.: An
488 inter-laboratory investigation of the Arctic sea ice biomarker proxy IP₂₅ in marine sediments: key outcomes
489 and recommendations, *Climate of the Past*, 10, 155-166, 10.5194/cp-10-155-2014, 2014.
- 490 Brassell, S. C., Eglinton, G., Marlowe, I. T., Pflaumann, U., and Sarinthein, M.: Molecular Stratigraphy - a New Tool for Climatic
491 Assessment, *Nature*, 320, 129-133, 10.1038/320129a0, 1986.
- 492 Brochier-Armanet, C., Boussau, B., Gribaldo, S., and Forterre, P.: Mesophilic Crenarchaeota: proposal for a third archaeal phylum, the
493 Thaumarchaeota, *Nat Rev Microbiol*, 6, 245-252, 10.1038/nrmicro1852, 2008.
- 494 Burke, K. D., Williams, J. W., Chandler, M. A., Haywood, A. M., Lunt, D. J., and Otto-Bliessner, B. L.: Pliocene and Eocene provide best
495 analogs for near-future climates, *Proc Natl Acad Sci U S A*, 115, 13288-13293, 10.1073/pnas.1809600115, 2018.
- 496 Caniupán, M., Lamy, F., Lange, C. B., Kaiser, J., Kilian, R., Arz, H. W., León, T., Mollenhauer, G., Sandoval, S., De Pol-Holz, R., Pantoja,
497 S., Wellner, J., and Tiedemann, R.: Holocene sea-surface temperature variability in the Chilean fjord region, *Quaternary Research*,
498 82, 342-353, 10.1016/j.yqres.2014.07.009, 2014.
- 499 Chong, P. L.: Archaeobacterial bipolar tetraether lipids: Physico-chemical and membrane properties, *Chem Phys Lipids*, 163, 253-265,
500 10.1016/j.chemphyslip.2009.12.006, 2010.
- 501 Conte, M. H., Sicre, M.-A., Rühlemann, C., Weber, J. C., Schulte, S., Schulz-Bull, D., and Blanz, T.: Global temperature calibration of the
502 alkenone unsaturation index (UK'37) in surface waters and comparison with surface sediments, *Geochemistry, Geophysics,*
503 *Geosystems*, 7, 10.1029/2005gc001054, 2006.
- 504 D'Hondt, S., Spivack, A. J., Pockalny, R., Ferdelman, T. G., Fischer, J. P., Kallmeyer, J., Abrams, L. J., Smith, D. C., Graham, D., Hasiuk,
505 F., Schrum, H., and Stancin, A. M.: Subseafloor sedimentary life in the South Pacific Gyre, *Proc Natl Acad Sci U S A*, 106, 11651-
506 11656, 10.1073/pnas.0811793106, 2009.
- 507 Dávila, P. M., Figueroa, D., and Müller, E.: Freshwater input into the coastal ocean and its relation with the salinity distribution off austral
508 Chile (35–55°S), *Continental Shelf Research*, 22, 521-534, 10.1016/s0278-4343(01)00072-3, 2002.
- 509 Dong, L., Li, Z. Y., and Jia, G. D.: Archaeal ammonia oxidation plays a part in late Quaternary nitrogen cycling in the South China Sea,
510 *Earth and Planetary Science Letters*, 509, 38-46, 10.1016/j.epsl.2018.12.023, 2019.
- 511 Durak, G. M., Taylor, A. R., Walker, C. E., Probert, I., de Vargas, C., Audic, S., Schroeder, D., Brownlee, C., and Wheeler, G. L.: A role
512 for diatom-like silicon transporters in calcifying coccolithophores, *Nat Commun*, 7, 10543, 10.1038/ncomms10543, 2016.
- 513 Elling, F. J., Konneke, M., Mussmann, M., Greve, A., and Hinrichs, K. U.: Influence of temperature, pH, and salinity on membrane lipid
514 composition and TEX86 of marine planktonic thaumarchaeal isolates, *Geochimica Et Cosmochimica Acta*, 171, 238-255,
515 10.1016/j.gca.2015.09.004, 2015.
- 516 Epstein, B. L., D'Hondt, S., and Hargraves, P. E.: The possible metabolic role of C37 alkenones in *Emiliania huxleyi*, *Organic Geochemistry*,
517 32, 867-875, 10.1016/s0146-6380(01)00026-2, 2001.
- 518 Fietz, S., Ho, S. L., and Hugué, C.: Archaeal Membrane Lipid-Based Paleothermometry for Applications in Polar Oceans, *Oceanography*,
519 33, 104-114, 10.5670/oceanog.2020.207, 2020.
- 520 Fietz, S., Ho, S. L., Hugué, C., Rosell-Mele, A., and Martínez-García, A.: Appraising GDGT-based seawater temperature indices in the
521 Southern Ocean, *Organic Geochemistry*, 102, 93-105, 10.1016/j.orggeochem.2016.10.003, 2016.
- 522 Fietz, S., Hugué, C., Rueda, G., Hambach, B., and Rosell-Mele, A.: Hydroxylated isoprenoidal GDGTs in the Nordic Seas, *Marine*
523 *Chemistry*, 152, 1-10, 10.1016/j.marchem.2013.02.007, 2013.

524 Gabriel, J. L. and Chong, P. L.: Molecular modeling of archaeobacterial bipolar tetraether lipid membranes, *Chem Phys Lipids*, 105, 193-
525 200, 10.1016/s0009-3084(00)00126-2, 2000.

526 Garreaud, R., Lopez, P., Minvielle, M., and Rojas, M.: Large-Scale Control on the Patagonian Climate, *Journal of Climate*, 26, 215-230,
527 10.1175/Jcli-D-12-00001.1, 2013.

528 Global_Modeling_and_Assimilation_Office_(GAMO): MERRA-2_tavgM_2d_adg_Nx: 2d,Monthly mean,Time-averaged,Single-
529 Level,Assimilation,Aerosol_Diagnostics (extended) V5.12.4 [dataset], 10.5067/RZIK2TV7PP38, 2015.

530 Herbert, T. D.: Review of alkenone calibrations (culture, water column, and sediments), *Geochemistry Geophysics Geosystems*, 2,
531 10.1029/2000gc000055, 2001.

532 Herbert, T. D.: Alkenone Paleotemperature Determinations, in: *Treatise on Geochemistry*, 399-433, 10.1016/b978-0-08-095975-7.00615-x,
533 2014.

534 Herbert, T. D., Peterson, L. C., Lawrence, K. T., and Liu, Z.: Tropical ocean temperatures over the past 3.5 million years, *Science*, 328,
535 1530-1534, 10.1126/science.1185435, 2010.

536 Hernández-Sánchez, M. T., Woodward, E. M. S., Taylor, K. W. R., Henderson, G. M., and Pancost, R. D.: Variations in GDGT distributions
537 through the water column in the South East Atlantic Ocean, *Geochimica et Cosmochimica Acta*, 132, 337-348,
538 10.1016/j.gca.2014.02.009, 2014.

539 Ho, S. L., Mollenhauer, G., Lamy, F., Martinez-Garcia, A., Mohtadi, M., Gersonde, R., Hebbeln, D., Nunez-Ricardo, S., Rosell-Mele, A.,
540 and Tiedemann, R.: Sea surface temperature variability in the Pacific sector of the Southern Ocean over the past 700 kyr,
541 *Paleoceanography*, 27, 10.1029/2012pa002317, 2012.

542 Ho, S. L., Mollenhauer, G., Fietz, S., Martinez-Garcia, A., Lamy, F., Rueda, G., Schipper, K., Meheust, M., Rosell-Mele, A., Stein, R., and
543 Tiedemann, R.: Appraisal of TEX86 and TEX86L thermometries in subpolar and polar regions, *Geochimica Et Cosmochimica Acta*,
544 131, 213-226, 10.1016/j.gca.2014.01.001, 2014.

545 Hopmans, E. C., Schouten, S., and Damste, J. S. S.: The effect of improved chromatography on GDGT-based palaeoproxies, *Organic*
546 *Geochemistry*, 93, 1-6, 10.1016/j.orggeochem.2015.12.006, 2016.

547 Hopmans, E. C., Weijers, J. W. H., Schefuss, E., Herfort, L., Damste, J. S. S., and Schouten, S.: A novel proxy for terrestrial organic matter
548 in sediments based on branched and isoprenoid tetraether lipids, *Earth and Planetary Science Letters*, 224, 107-116,
549 10.1016/j.epsl.2004.05.012, 2004.

550 Huguet, C., Fietz, S., and Rosell-Mele, A.: Global distribution patterns of hydroxy glycerol dialkyl glycerol tetraethers, *Organic*
551 *Geochemistry*, 57, 107-118, 10.1016/j.orggeochem.2013.01.010, 2013.

552 Jaeschke, A., Wengler, M., Hefter, J., Ronge, T. A., Geibert, W., Mollenhauer, G., Gersonde, R., and Lamy, F.: A biomarker perspective on
553 dust, productivity, and sea surface temperature in the Pacific sector of the Southern Ocean, *Geochimica Et Cosmochimica Acta*, 204,
554 120-139, 10.1016/j.gca.2017.01.045, 2017.

555 Kaiser, J., Schouten, S., Kilian, R., Arz, H. W., Lamy, F., and Damste, J. S. S.: Isoprenoid and branched GDGT-based proxies for surface
556 sediments from marine, fjord and lake environments in Chile, *Organic Geochemistry*, 89-90, 117-127,
557 10.1016/j.orggeochem.2015.10.007, 2015.

558 Kalanetra, K. M., Bano, N., and Hollibaugh, J. T.: Ammonia-oxidizing Archaea in the Arctic Ocean and Antarctic coastal waters, *Environ*
559 *Microbiol*, 11, 2434-2445, 10.1111/j.1462-2920.2009.01974.x, 2009.

560 Karner, M. B., DeLong, E. F., and Karl, D. M.: Archaeal dominance in the mesopelagic zone of the Pacific Ocean, *Nature*, 409, 507-510,
561 10.1038/35054051, 2001.

562 Kim, J. H., Villanueva, L., Zell, C., and Damste, J. S. S.: Biological source and provenance of deep-water derived isoprenoid tetraether lipids
563 along the Portuguese continental margin, *Geochimica Et Cosmochimica Acta*, 172, 177-204, 10.1016/j.gca.2015.09.010, 2016.

564 Kim, J. H., Romero, O. E., Lohmann, G., Donner, B., Laepple, T., Haam, E., and Damste, J. S. S.: Pronounced subsurface cooling of North
565 Atlantic waters off Northwest Africa during Dansgaard-Oeschger interstadials, *Earth and Planetary Science Letters*, 339, 95-102,
566 10.1016/j.epsl.2012.05.018, 2012a.

567 Kim, J. H., Crosta, X., Willmott, V., Renssen, H., Bonnin, J., Helmke, P., Schouten, S., and Damste, J. S. S.: Holocene subsurface temperature
568 variability in the eastern Antarctic continental margin, *Geophysical Research Letters*, 39, 10.1029/2012gl051157, 2012b.

569 Kim, J. H., van der Meer, J., Schouten, S., Helmke, P., Willmott, V., Sangiorgi, F., Koc, N., Hopmans, E. C., and Damste, J. S. S.: New
570 indices and calibrations derived from the distribution of crenarchaeal isoprenoid tetraether lipids: Implications for past sea surface
571 temperature reconstructions, *Geochimica Et Cosmochimica Acta*, 74, 4639-4654, 10.1016/j.gca.2010.05.027, 2010.

572 Kim, J. H., Schouten, S., Rodrigo-Gamiz, M., Rampen, S., Marino, G., Huguet, C., Helmke, P., Buscail, R., Hopmans, E. C., Pross, J.,
573 Sangiorgi, F., Middelburg, J. B. M., and Damste, J. S. S.: Influence of deep-water derived isoprenoid tetraether lipids on the TEX86H
574 paleothermometer in the Mediterranean Sea, *Geochimica Et Cosmochimica Acta*, 150, 125-141, 10.1016/j.gca.2014.11.017, 2015.

575 Koenig, Z., Provost, C., Ferrari, R., Sennechael, N., and Rio, M. H.: Volume transport of the Antarctic Circumpolar Current: Production and
576 validation of a 20 year long time series obtained from in situ and satellite observations, *Journal of Geophysical Research-Oceans*,
577 119, 5407-5433, 10.1002/2014jc009966, 2014.

578 Lamping, N., Muller, J., Hefter, J., Mollenhauer, G., Haas, C., Shi, X. X., Vorrath, M. E., Lohmann, G., and Hillenbrand, C. D.: Evaluation
579 of lipid biomarkers as proxies for sea ice and ocean temperatures along the Antarctic continental margin, *Climate of the Past*, 17,
580 2305-2326, 10.5194/cp-17-2305-2021, 2021.

581 Lamy, F.: The Expedition PS97 of the Research Vessel POLARSTERN to the Drake Passage in 2016 , *Berichte zur Polar- und*
582 *Meeresforschung = Reports on polar and marine research*, Bremerhaven, Alfred Wegener Institute for Polar and Marine Research,
583 571 p., http://doi.org/10.2312/BzPM_0701_2016, 2016.

584 Lamy, F., Kilian, R., Arz, H. W., Francois, J. P., Kaiser, J., Prange, M., and Steinke, T.: Holocene changes in the position and intensity of
585 the northern westerly wind belt, *Nature Geoscience*, 3, 695-699, 10.1038/Ngeo959, 2010.

586 Lamy, F., Gersonde, R., Winckler, G., Esper, O., Jaeschke, A., Kuhn, G., Ullermann, J., Martinez-Garcia, A., Lambert, F., and Kilian, R.:
587 Increased dust deposition in the Pacific Southern Ocean during glacial periods, *Science*, 343, 403-407, 10.1126/science.1245424,
588 2014.

589 Liu, R. J., Han, Z. B., Zhao, J., Zhang, H. F., Li, D., Ren, J. Y., Pan, J. M., and Zhang, H. S.: Distribution and source of glycerol dialkyl
590 glycerol tetraethers (GDGTs) and the applicability of GDGT-based temperature proxies in surface sediments of Prydz Bay, East
591 Antarctica, *Polar Research*, 39, 10.33265/polar.v39.3557, 2020.

592 Locarnini, R. A., Mishonov, A. V., Antonov, J. I., Boyer, T. P., and Garcia, H. E.: *World Ocean Atlas 2005, Volume 1: Temperature*, S.
593 Levitus, Ed. NOAA Atlas NESDIS 61 [dataset], 2006.

594 Locarnini, R. A., Mishonov, A. V., Antonov, J. I., Boyer, T. P., Garcia, H. E., Baranova, O. K., Zweng, M. M., and Johnson, D. R.: *World*
595 *Ocean Atlas 2009, Volume 1: Temperature* S. Levitus, Ed., NOAA Atlas NESIDIS 68, U.S. Government Printing Office,
596 Washington, D.C., 184 pp., 2010.

597 Lü, X., Liu, X.-L., Elling, F. J., Yang, H., Xie, S., Song, J., Li, X., Yuan, H., Li, N., and Hinrichs, K.-U.: Hydroxylated isoprenoid GDGTs
598 in Chinese coastal seas and their potential as a paleotemperature proxy for mid-to-low latitude marginal seas, *Organic Geochemistry*,
599 89-90, 31-43, 10.1016/j.orggeochem.2015.10.004, 2015.

600 Massana, R., Taylor, L. J., Murray, A. E., Wu, K. Y., Jeffrey, W. H., and DeLong, E. F.: Vertical distribution and temporal variation of
601 marine planktonic archaea in the Gerlache Strait, Antarctica, during early spring, *Limnology and Oceanography*, 43, 607-617,
602 10.4319/lo.1998.43.4.0607, 1998.

603 Max, L., Lembke-Jene, L., Zou, J., Shi, X., and Tiedemann, R.: Evaluation of reconstructed sea surface temperatures based on U37k' from
604 sediment surface samples of the North Pacific, *Quaternary Science Reviews*, 243, 10.1016/j.quascirev.2020.106496, 2020.

605 Méheust, M., Fahl, K., and Stein, R.: Variability in modern sea surface temperature, sea ice and terrigenous input in the sub-polar North
606 Pacific and Bering Sea: Reconstruction from biomarker data, *Organic Geochemistry*, 57, 54-64, 10.1016/j.orggeochem.2013.01.008,
607 2013.

608 Müller, P. J., Kirst, G., Ruhland, G., von Storch, I., and Rosell-Melé, A.: Calibration of the alkenone paleotemperature index U37k' based
609 on core-tops from the eastern South Atlantic and the global ocean (60°N-60°S), *Geochimica et Cosmochimica Acta*, 62, 1757-1772,
610 10.1016/s0016-7037(98)00097-0, 1998.

611 Murray, A. E., Preston, C. M., Massana, R., Taylor, L. T., Blakis, A., Wu, K., and DeLong, E. F.: Seasonal and spatial variability of bacterial
612 and archaeal assemblages in the coastal waters near Anvers Island, Antarctica, *Appl Environ Microbiol*, 64, 2585-2595,
613 10.1128/AEM.64.7.2585-2595.1998, 1998.

614 Orsi, A. H., Whitworth, T., and Nowlin, W. D.: On the Meridional Extent and Fronts of the Antarctic Circumpolar Current, *Deep-Sea*
615 *Research Part I-Oceanographic Research Papers*, 42, 641-673, 10.1016/0967-0637(95)00021-W, 1995.

616 Pearson, A. and Ingalls, A. E.: Assessing the Use of Archaeal Lipids as Marine Environmental Proxies, *Annual Review of Earth and*
617 *Planetary Sciences*, Vol 41, 41, 359-384, 10.1146/annurev-earth-050212-123947, 2013.

618 Popp, B. N., Kenig, F., Wakeham, S. G., Laws, E. A., and Bidigare, R. R.: Does growth rate affect ketone unsaturation and intracellular
619 carbon isotopic variability in *Emiliania huxleyi*?, *Paleoceanography*, 13, 35-41, 10.1029/97pa02594, 1998.

620 Prahl, F. G. and Wakeham, S. G.: Calibration of unsaturation patterns in long-chain ketone compositions for palaeotemperature assessment,
621 *Nature*, 330, 367-369, 10.1038/330367a0, 1987.

622 Prahl, F. G., Mix, A. C., and Sparrow, M. A.: Alkenone paleothermometry: Biological lessons from marine sediment records off western
623 South America, *Geochimica Et Cosmochimica Acta*, 70, 101-117, 10.1016/j.gca.2005.08.023, 2006.

624 Prahl, F. G., Muehlhausen, L. A., and Zahnle, D. L.: Further Evaluation of Long-Chain Alkenones as Indicators of Paleoceanographic
625 Conditions, *Geochimica Et Cosmochimica Acta*, 52, 2303-2310, 10.1016/0016-7037(88)90132-9, 1988.

626 Prahl, F. G., Rontani, J. F., Zabeti, N., Walinsky, S. E., and Sparrow, M. A.: Systematic pattern in U-37(K') - Temperature residuals for
627 surface sediments from high latitude and other oceanographic settings, *Geochimica Et Cosmochimica Acta*, 74, 131-143,
628 10.1016/j.gca.2009.09.027, 2010.

629 Qin, W., Carlson, L. T., Armbrust, E. V., Devol, A. H., Moffett, J. W., Stahl, D. A., and Ingalls, A. E.: Confounding effects of oxygen and
630 temperature on the TEX86 signature of marine Thaumarchaeota, *Proc Natl Acad Sci U S A*, 112, 10979-10984,
631 10.1073/pnas.1501568112, 2015.

632 Quiñones, R. A., Levipan, H. A., and Urrutia, H.: Spatial and temporal variability of planktonic archaeal abundance in the Humboldt Current
633 System off Chile, *Deep Sea Research Part II: Topical Studies in Oceanography*, 56, 1073-1082, 10.1016/j.dsr2.2008.09.012, 2009.

634 Rintoul, S. R.: The global influence of localized dynamics in the Southern Ocean, *Nature*, 558, 209-218, 10.1038/s41586-018-0182-3, 2018.

635 Saavedra-Pellitero, M., Baumann, K. H., Flores, J. A., and Gersonde, R.: Biogeographic distribution of living coccolithophores in the Pacific
636 sector of the Southern Ocean, *Marine Micropaleontology*, 109, 1-20, 10.1016/j.marmicro.2014.03.003, 2014.

637 Saavedra-Pellitero, M., Baumann, K. H., Fuertes, M. A., Schulz, H., Marcon, Y., Vollmar, N. M., Flores, J. A., and Lamy, F.: Calcification
638 and latitudinal distribution of extant coccolithophores across the Drake Passage during late austral summer 2016, *Biogeosciences*,
639 16, 3679-3702, 10.5194/bg-16-3679-2019, 2019.

640 Schneider, C., Glaser, M., Kilian, R., Santana, A., Butorovic, N., and Casassa, G.: Weather Observations Across the Southern Andes at 53°S,
641 *Physical Geography*, 24, 97-119, 10.2747/0272-3646.24.2.97, 2003.

642 Schouten, S., Hopmans, E. C., and Damste, J. S. S.: The organic geochemistry of glycerol dialkyl glycerol tetraether lipids: A review,
643 *Organic Geochemistry*, 54, 19-61, 10.1016/j.orggeochem.2012.09.006, 2013a.

644 Schouten, S., Hopmans, E. C., Schefuß, E., and Sinninghe Damsté, J. S.: Distributional variations in marine crenarchaeotal membrane lipids:
645 a new tool for reconstructing ancient sea water temperatures?, *Earth and Planetary Science Letters*, 204, 265-274, 10.1016/s0012-
646 821x(02)00979-2, 2002.

647 Schouten, S., Hugué, C., Hopmans, E. C., Kienhuis, M. V., and Damste, J. S.: Analytical methodology for TEX86 paleothermometry by
648 high-performance liquid chromatography/atmospheric pressure chemical ionization-mass spectrometry, *Anal Chem*, 79, 2940-2944,
649 10.1021/ac062339v, 2007.

650 Schouten, S., Pitcher, A., Hopmans, E. C., Villanueva, L., van Bleijswijk, J., and Damste, J. S. S.: Intact polar and core glycerol dibiphytanyl
651 glycerol tetraether lipids in the Arabian Sea oxygen minimum zone: I. Selective preservation and degradation in the water column
652 and consequences for the TEX86, *Geochimica Et Cosmochimica Acta*, 98, 228-243, 10.1016/j.gca.2012.05.002, 2012.

653 Schouten, S., Hopmans, E. C., Rosell-Melé, A., Pearson, A., Adam, P., Bauersachs, T., Bard, E., Bernasconi, S. M., Bianchi, T. S., Brocks,
654 J. J., Carlson, L. T., Castañeda, I. S., Derenne, S., Selver, A. D., Dutta, K., Eglinton, T., Fosse, C., Galy, V., Grice, K., Hinrichs, K.-
655 U., Huang, Y., Hugué, A., Hugué, C., Hurley, S., Ingalls, A., Jia, G., Keely, B., Knappy, C., Kondo, M., Krishnan, S., Lincoln, S.,
656 Lipp, J., Mangelsdorf, K., Martínez-García, A., Ménot, G., Mets, A., Mollenhauer, G., Ohkouchi, N., Ossebaar, J., Pagani, M.,
657 Pancost, R. D., Pearson, E. J., Peterse, F., Reichart, G.-J., Schaeffer, P., Schmitt, G., Schwark, L., Shah, S. R., Smith, R. W.,
658 Smittenberg, R. H., Summons, R. E., Takano, Y., Talbot, H. M., Taylor, K. W. R., Tarozo, R., Uchida, M., van Dongen, B. E., Van
659 Mooy, B. A. S., Wang, J., Warren, C., Weijers, J. W. H., Werne, J. P., Woltering, M., Xie, S., Yamamoto, M., Yang, H., Zhang, C.
660 L., Zhang, Y., Zhao, M., and Damsté, J. S. S.: An interlaboratory study of TEX86 and BIT analysis of sediments, extracts, and
661 standard mixtures, *Geochemistry, Geophysics, Geosystems*, 14, 5263-5285, 10.1002/2013gc004904, 2013b.

662 Sikes, E. L., Volkman, J. K., Robertson, L. G., and Pichon, J. J.: Alkenones and alkenes in surface waters and sediments of the Southern
663 Ocean: Implications for paleotemperature estimation in polar regions, *Geochimica Et Cosmochimica Acta*, 61, 1495-1505,
664 10.1016/S0016-7037(97)00017-3, 1997.

665 Smith, H. E. K., Poulton, A. J., Garley, R., Hopkins, J., Lubelczyk, L. C., Drapeau, D. T., Rauschenberg, S., Twining, B., Bates, N. R., and
666 Balch, W. M.: The influence of environmental variability on the biogeography of coccolithophores and diatoms in the Great Calcite
667 Belt, *Biogeosciences*, 14, 4905-4925, 10.5194/bg-14-4905-2017, 2017.

668 Strub, P. T., Mesias, J. M., Montecino, V., Ruttlant, J., and Salinas, S.: Chapter 10. Coastal ocean circulation off western south america
669 coastal segment, in: *The Sea*, edited by: Robinson, A. R., and Kenneth, H. B., 273-313, 1998.

670 Taylor, K. W. R., Huber, M., Hollis, C. J., Hernandez-Sanchez, M. T., and Pancost, R. D.: Re-evaluating modern and Palaeogene GDGT
671 distributions: Implications for SST reconstructions, *Global and Planetary Change*, 108, 158-174, 10.1016/j.gloplacha.2013.06.011,
672 2013.

673 Toyos, M. H., Winckler, G., Arz, H. W., Lembke-Jene, L., Lange, C. B., Kuhn, G., and Lamy, F.: Variations in export production, lithogenic
674 sediment transport and iron fertilization in the Pacific sector of the Drake Passage over the past 400 kyr, *Climate of the Past*, 18,
675 147-166, 10.5194/cp-18-147-2022, 2022.

676 Tyrrell, T. and Merico, A.: *Emiliania huxleyi*: bloom observations and the conditions that induce them, in: *Coccolithophores*, 75-97,
677 10.1007/978-3-662-06278-4_4, 2004.

678 Villanueva, L., Schouten, S., and Sinninghe Damsté, J. S.: Depth-related distribution of a key gene of the tetraether lipid biosynthetic pathway
679 in marine Thaumarchaeota, *Environ Microbiol*, 17, 3527-3539, 10.1111/1462-2920.12508, 2015.

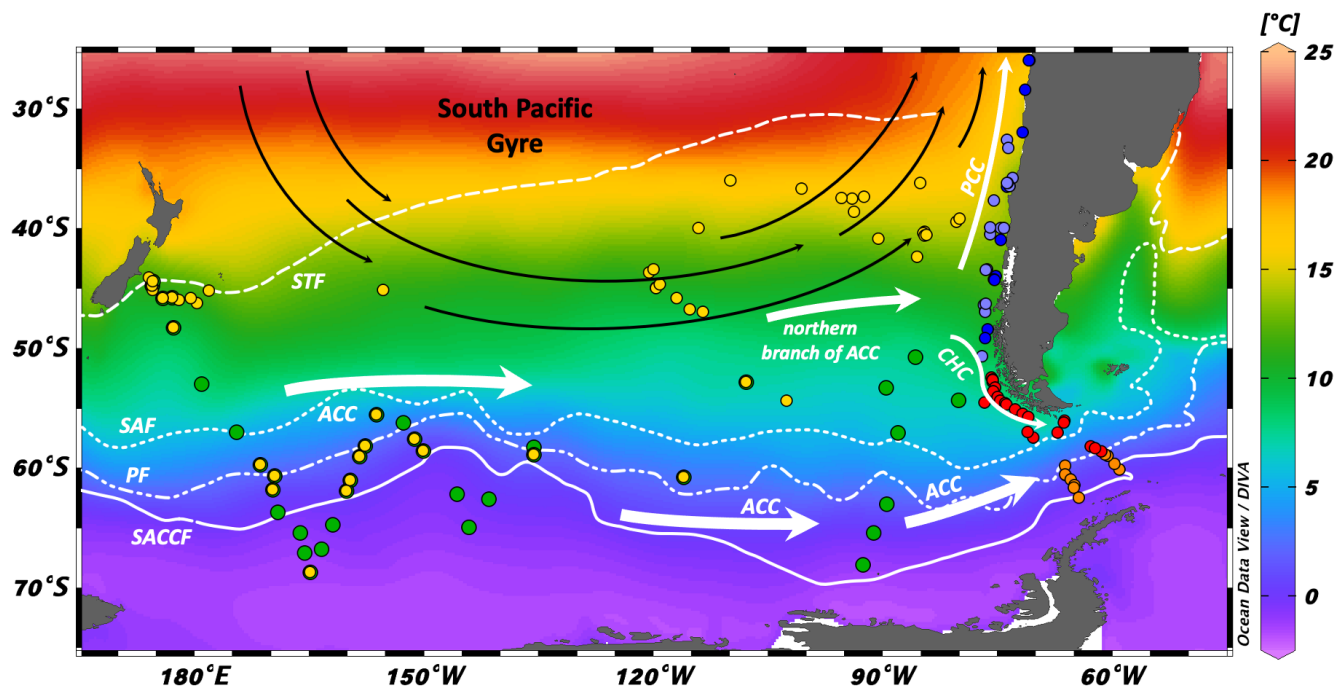
680 Volkman, J. K.: Ecological and environmental factors affecting alkenone distributions in seawater and sediments, *Geochemistry Geophysics*
681 *Geosystems*, 1, n/a-n/a, 10.1029/2000gc000061, 2000.

682 Vollmar, N. M., Baumann, K. H., Saavedra-Pellitero, M., and Hernandez-Almeida, I.: Distribution of coccoliths in surface sediments across
683 the Drake Passage and calcification of *Emiliania huxleyi* morphotypes, *Biogeosciences*, 19, 585-612, 10.5194/bg-19-585-2022,
684 2022.

685 Vorrath, M. E., Muller, J., Rebolledo, L., Cardenas, P., Shi, X. X., Esper, O., Opel, T., Geibert, W., Munoz, P., Haas, C., Kuhn, G., Lange,
686 C. B., Lohmann, G., and Mollenhauer, G.: Sea ice dynamics in the Bransfield Strait, Antarctic Peninsula, during past 240 years: a
687 multi-proxy intercomparison study, *Climate of the Past*, 16, 2459-2483, 10.5194/cp-16-2459-2020, 2020.

688 Watson, A. J., Vallis, G. K., and Nikurashin, M.: Southern Ocean buoyancy forcing of ocean ventilation and glacial atmospheric CO₂,
689 *Nature Geoscience*, 8, 10.1038/Ngeo2538, 2015.

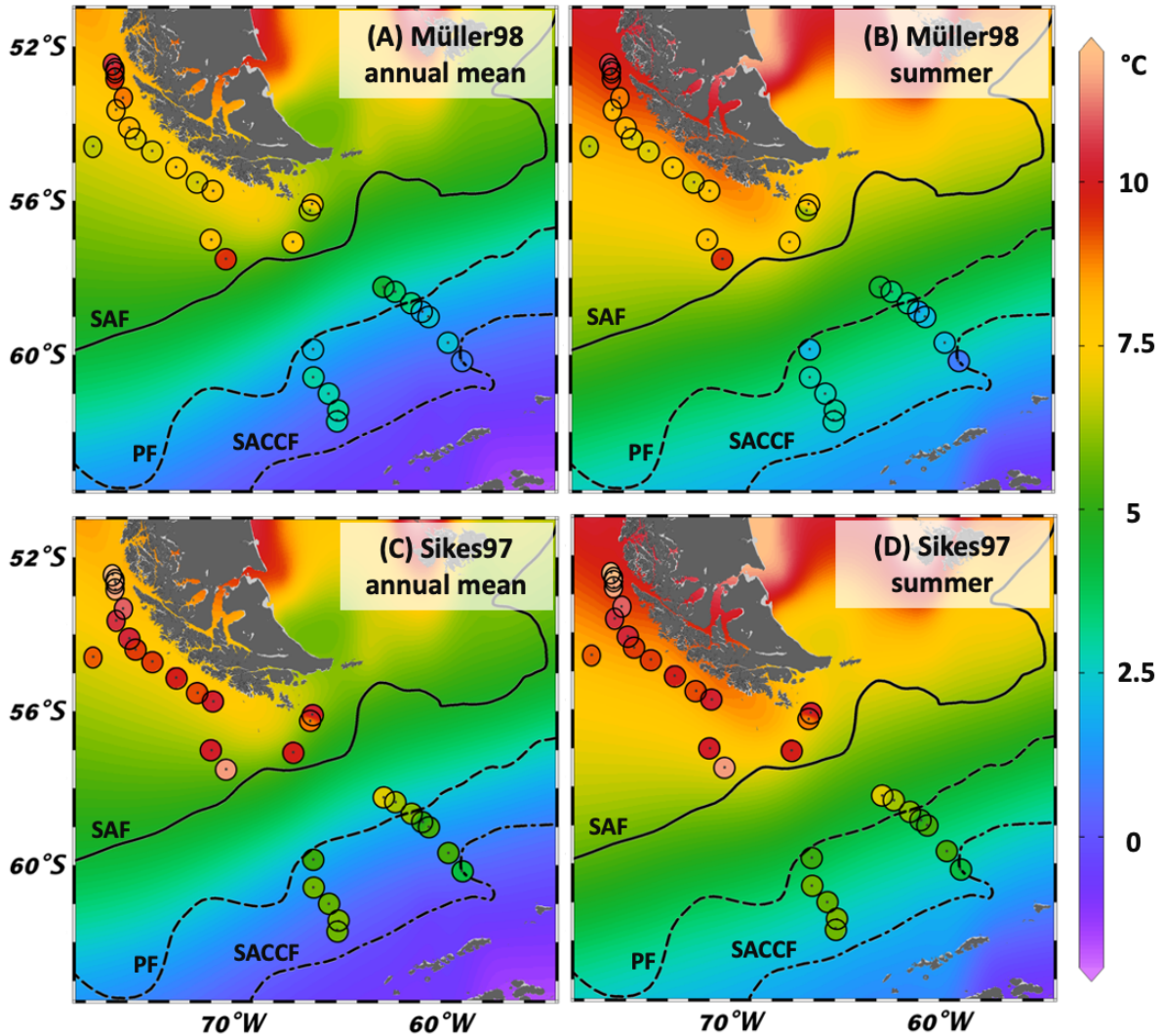
690 Weijers, J. W. H., Schouten, S., Spaargaren, O. C., and Damste, J. S. S.: Occurrence and distribution of tetraether membrane lipids in soils:
691 Implications for the use of the TEX86 proxy and the BIT index, *Organic Geochemistry*, 37, 1680-1693,
692 10.1016/j.orggeochem.2006.07.018, 2006.
693 Wuchter, C., Schouten, S., Wakeham, S. G., and Sinninghe Damsté, J. S.: Temporal and spatial variation in tetraether membrane lipids of
694 marine Crenarchaeota in particulate organic matter: Implications for TEX86paleothermometry, *Paleoceanography*, 20,
695 10.1029/2004pa001110, 2005.
696



697

698 Figure 1: Map with SSTs (WOA05; Locarnini et al., 2006) of the extended study area and sample locations. ACC: Antarctic
 699 Circumpolar Current; PCC: Peru-Chile Current; CHC: Cape Horn Current; STF: Subtropical Front; SAF: Subantarctic Front;
 700 PF: Polar Front; SACCF: Southern ACC Front. Red dots: Southern Chilean Margin and Drake Passage samples (this study);
 701 Orange dots: Drake Passage samples (Lamping et al., 2021; this study); Light blue dots: Northern – Central Chilean Margin samples
 702 (Prahl et al., 2006; Prahl et al., 2010); Dark blue dots: Northern – Central Chilean Margin samples (Kaiser et al., 2015); Yellow dots:
 703 South Pacific Gyre, Central South Pacific and New Zealand Margin samples (Jaeschke et al., 2017); Green dots: Central South
 704 Pacific and New Zealand Margin samples (Ho et al., 2014).

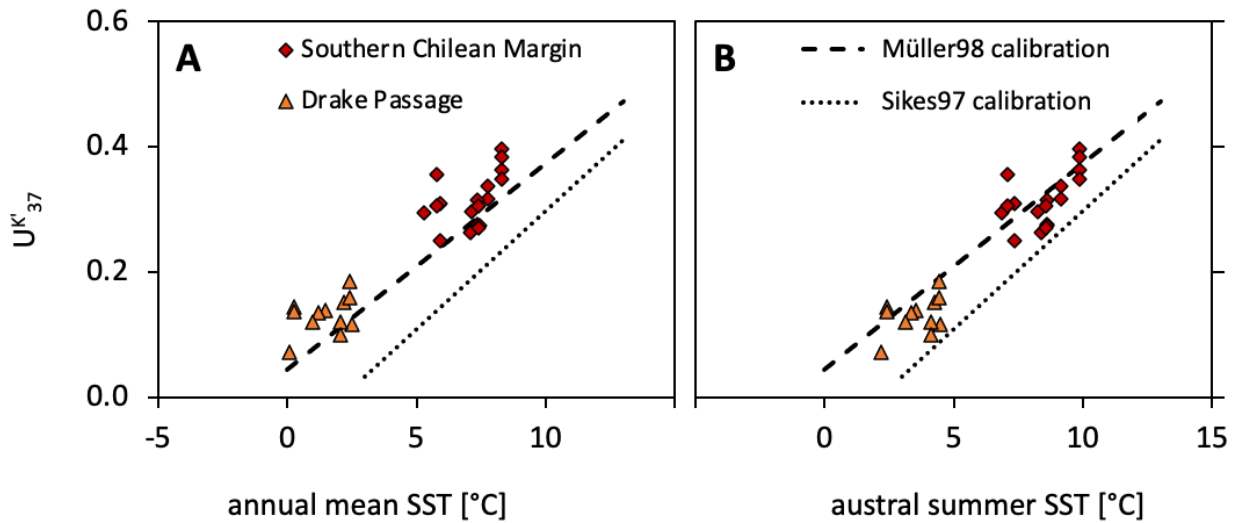
705



706

707 **Figure 2: Map of reconstructed SST values for $U^{K'}_{37}$ (this study). Background gridded temperatures: WOA05 data (WOA05;**
 708 **Locarnini et al., 2006), colored dots are calculated SSTs. (A) WOA05 annual mean SSTs with Müller98 calibration; (B) WOA05**
 709 **summer SSTs with Müller98 calibration; (C) WOA05 annual mean SSTs with Sikes97 calibration; (D) WOA05 summer SSTs with**
 710 **Sikes97 calibration.**

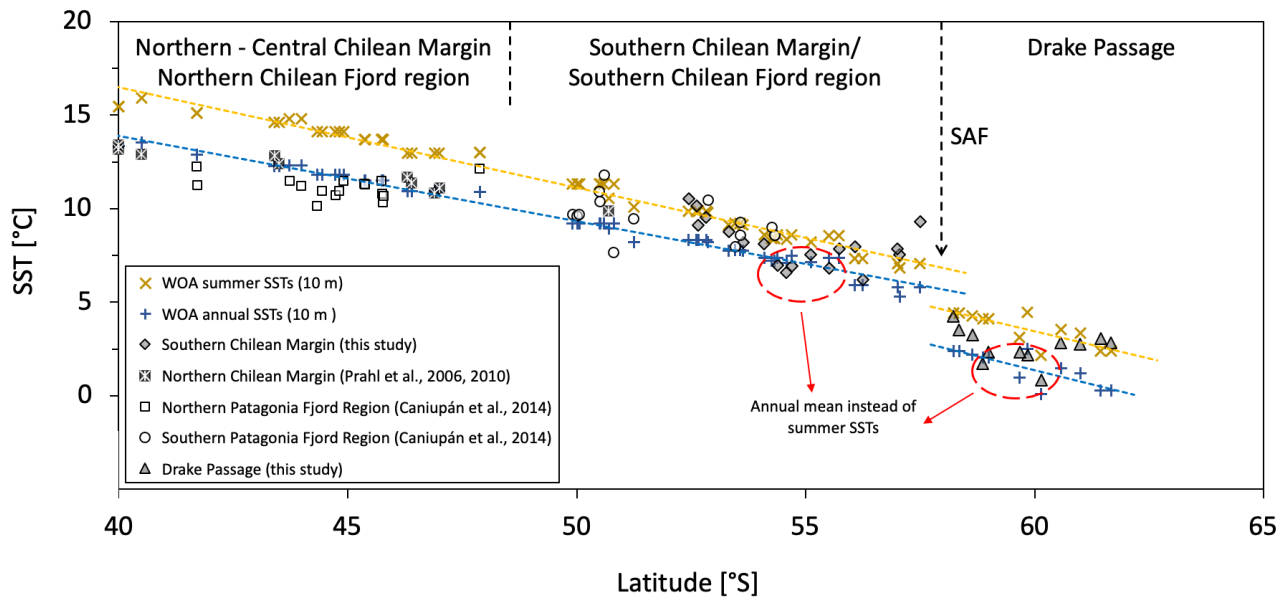
711



712

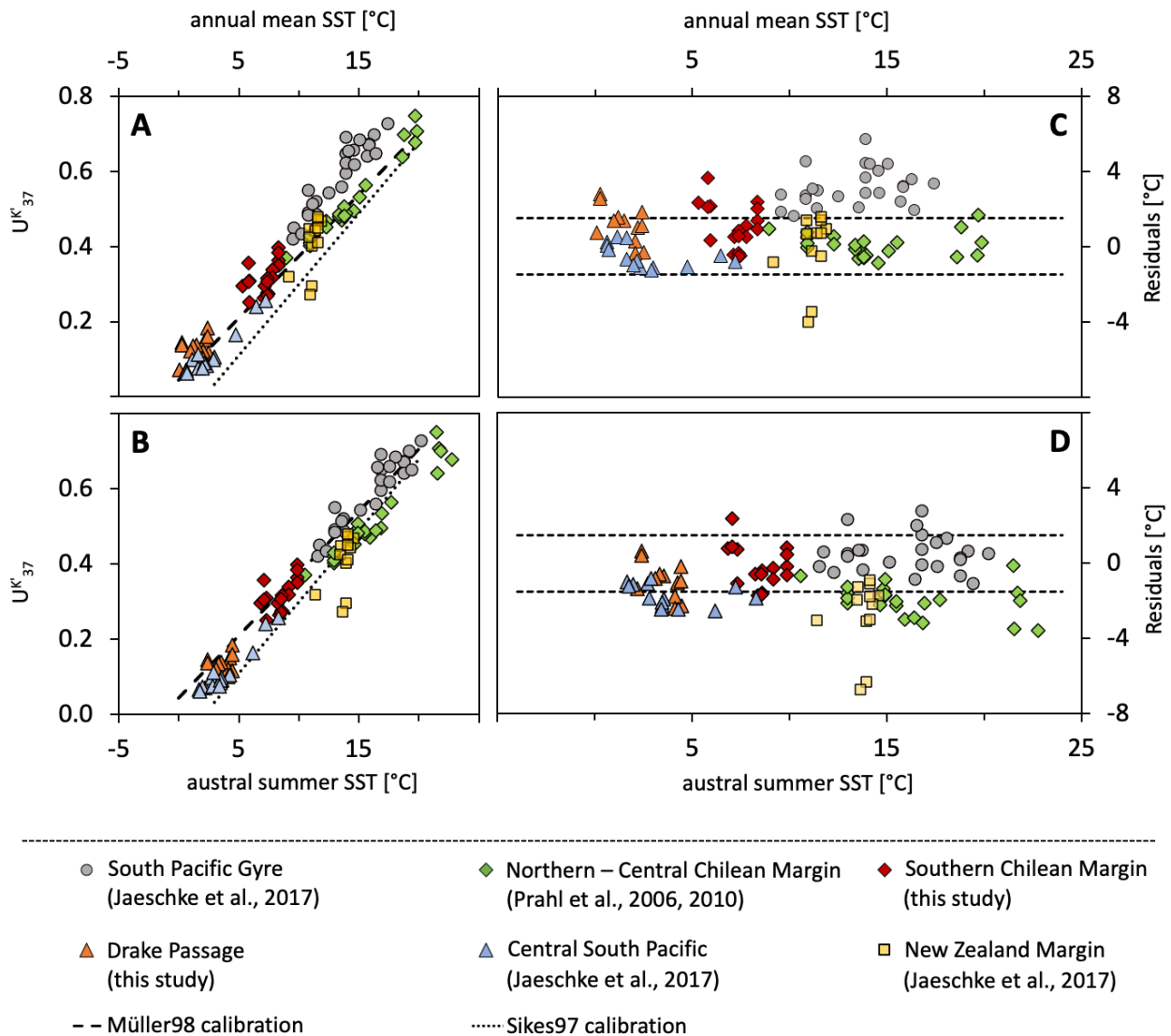
713 **Figure 3: Comparison of U^{K}_{37} index (this study) with modern SSTs at 10 m water depth (WOA05; Locarnini et al., 2006), for (A)**
 714 **annual mean SSTs, and (B) austral summer SSTs, corresponding to January – March.**

715



716

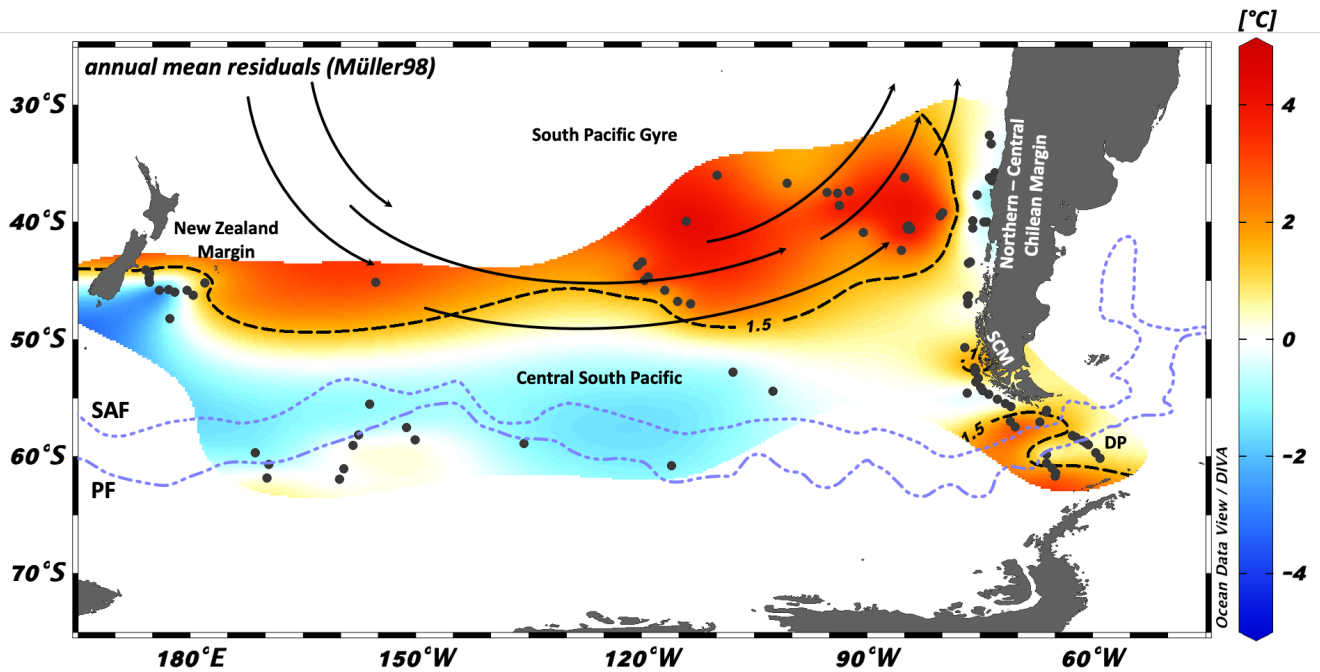
717 **Figure 4: Comparison of ocean and fjord samples in the Chilean region. Yellow and Blue dashed lines show the meridional**
 718 **temperature evolution during summer and annual mean at 10 m water depth, respectively. Annual mean and summer data were**
 719 **taken from WOA09 (Locarnini et al., 2010) for the samples of Caniupán et al. (2014) and WOA05 (Locarnini et al., 2006) for Prah**
 720 **et al. (2006, 2010) and this study.**



722

723 **Figure 5: (A) and (B):** Compilation of $U^{K_{37}}$ index of this study and the expanded South Pacific study area with SSTs at 10 m water
 724 **depth** for annual mean and austral summer, respectively (WOA05; Locarnini et al., 2006). (C) and (D): Residuals of the local SSTs
 725 **at 10 m water depth** for the annual mean and austral summer (WOA05; Locarnini et al., 2006) subtracted by the Müller98 calculated
 726 **SSTs**. Temperature range of dotted line shows the standard error of the temperature calibration of $\pm 1.5^\circ \text{C}$ by Müller et al. (1998).
 727 **Site PS75/088-6 (Jaeschke et al., 2017) was excluded** due to unrealistic high temperatures of $>10^\circ \text{C}$.

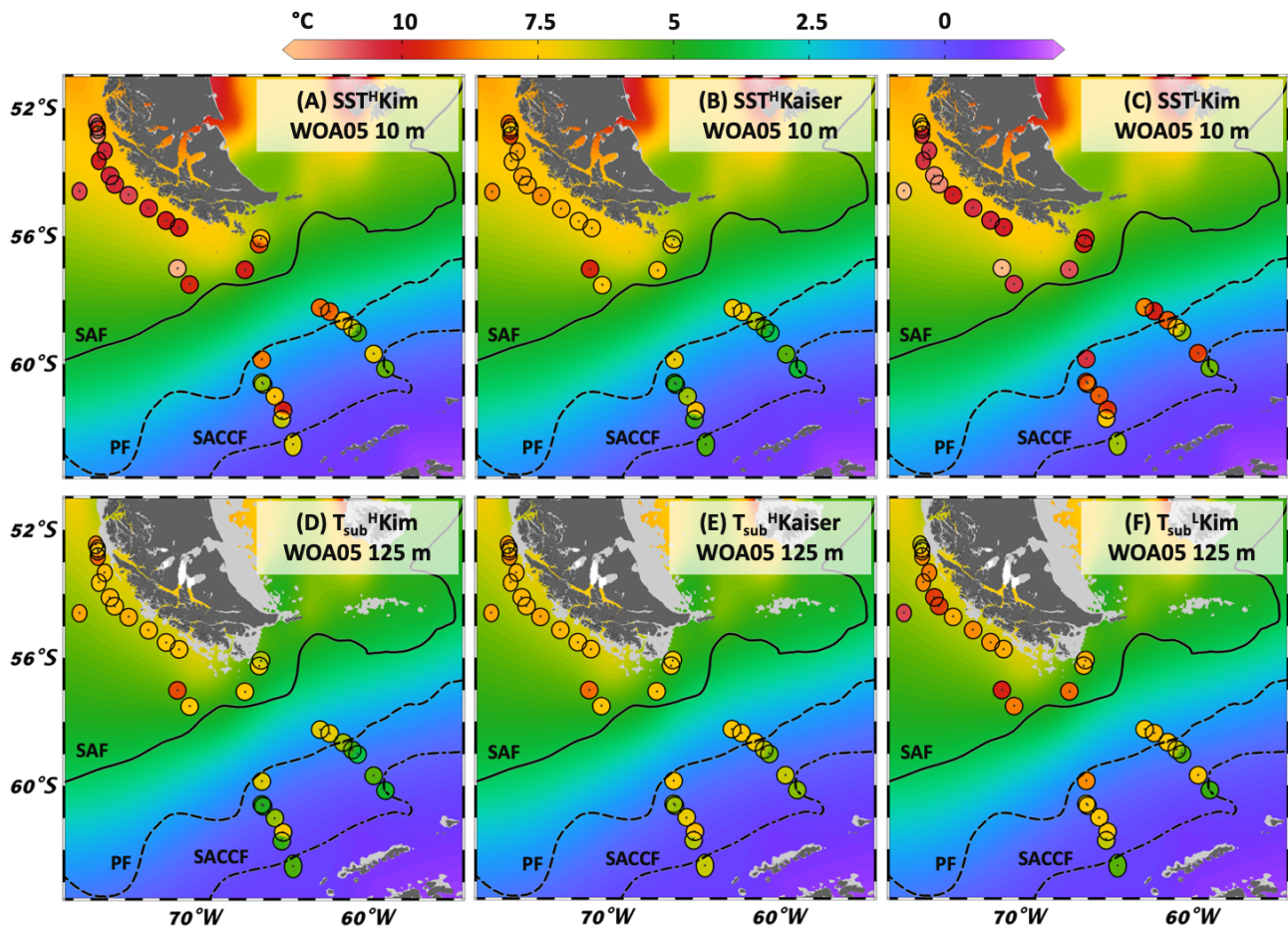
728



729

730 Figure 6: Map with residuals for the extended study area of the South Pacific with published data from the Central South Pacific,
 731 the New Zealand Margin, the South Pacific Gyre (Jaeschke et al., 2017) and the Chilean Margin (Prah et al., 2006; this study; Prah
 732 et al., 2010). Atlas-derived annual mean WOA05 water temperatures of 10 m water depth (Locarnini et al., 2006) were subtracted
 733 from the SST Müller98 calibration. SCM: Southern Chilean Margin; DP: Drake Passage; SAF: Subantarctic Front; PF: Polar
 734 Front.

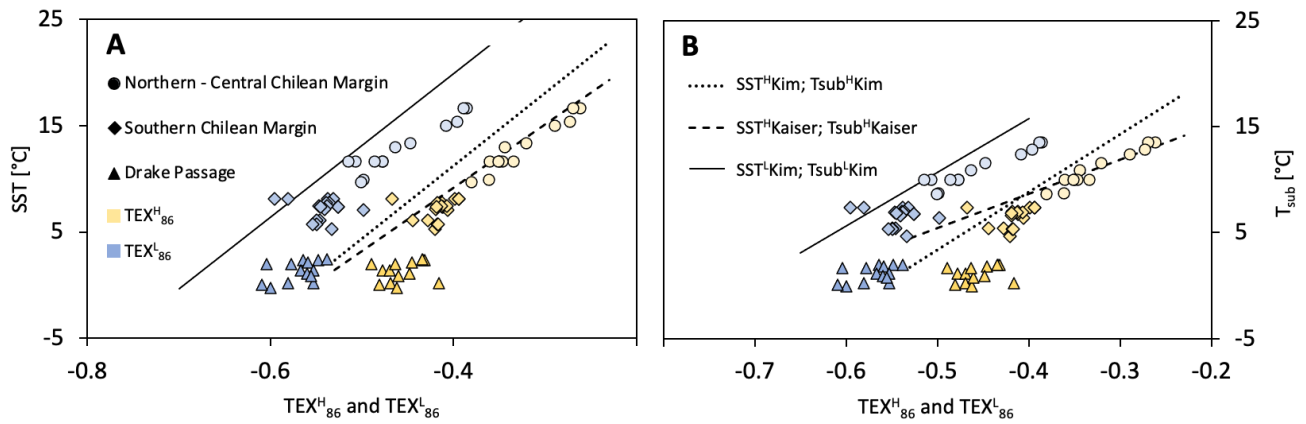
735



736

737 **Figure 7: Map of reconstructed SST and Tsub values for TEX^H₈₆ and TEX^L₈₆ (this study). Background gridded annual mean**
 738 **temperatures at 10 or 125 m water depth: WOA05 data, colored dots are calculated SSTs or Tsub. (A) WOA05 SSTs with calculated**
 739 **data after SST^HKim; (B) WOA05 SSTs with calculated data after SST^HKaiser; (C) WOA05 SSTs with calculated data after**
 740 **SST^LKim; (D) WOA05 Tsub with calculated data after Tsub^HKim; (E) WOA05 Tsub with calculated data after Tsub^HKaiser; (F)**
 741 **WOA05 Tsub with calculated data after Tsub^LKim.**

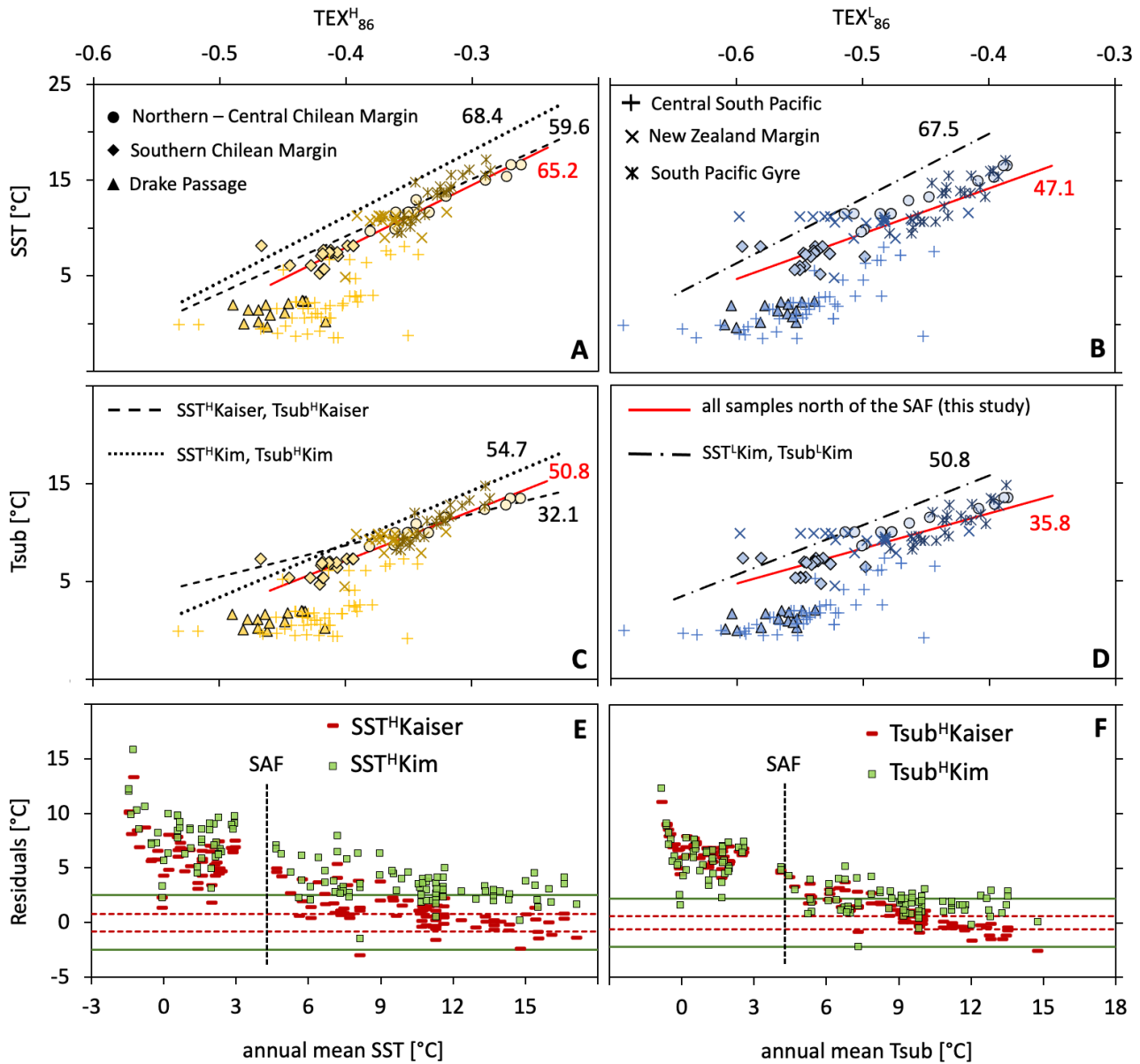
742



743

744 **Figure 8: Comparison of TEX_{86}^L (blue) and TEX_{86}^H (yellow) data with water temperature with the SST 0 – 50 m water depth and**
 745 **Tsub 0 – 200 m (WOA05; Locarnini et al., 2006), respectively. Black line: TEX_{86}^L calibration line (SST^LKim, Tsub^LKim) for surface**
 746 **and subsurface, respectively. Circles: Kaiser et al. (2015); Route: this study; triangle: Lamping et al. (2021) and this study.**

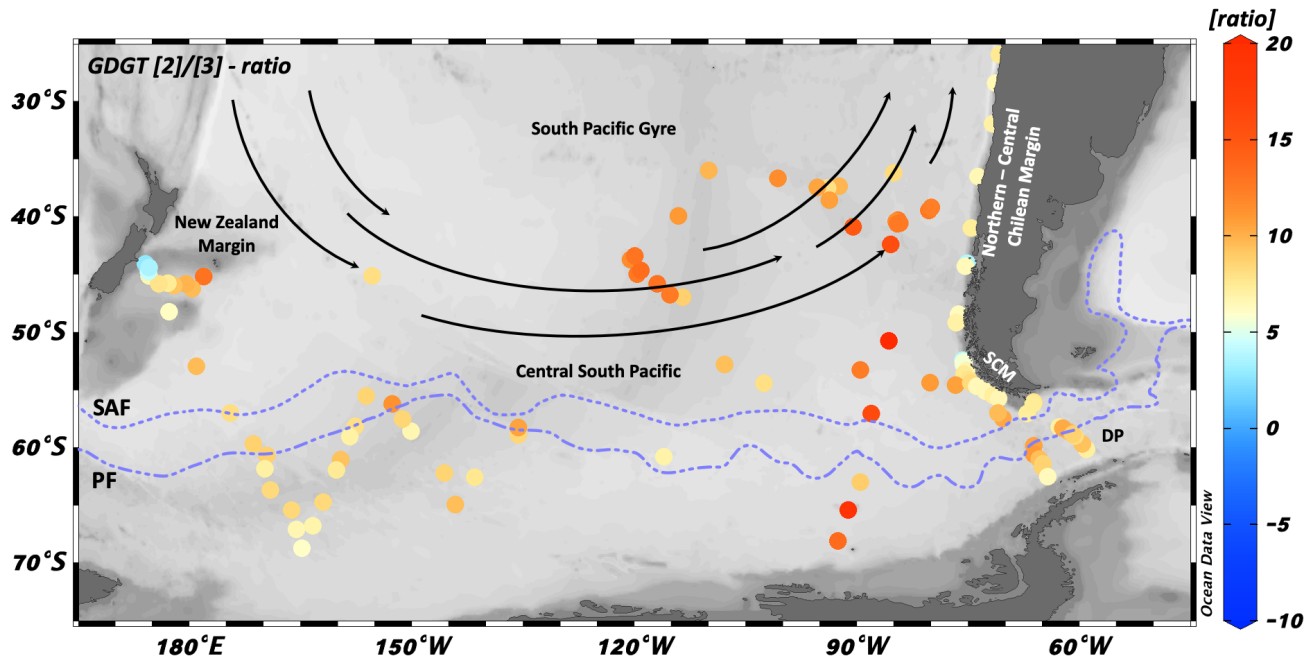
747



748

749 **Figure 9:** (A) – (D): Comparison of TEX₈₆^H (yellow) and TEX₈₆^L (blue) data with annual mean water temperature with the SST 0 –
 750 50 m water depth and Tsub 0 – 200 m (WOA05; Locarnini et al., 2006), respectively. The black (previous studies) and red numbers
 751 (this study) indicate the slope of the corresponding calibration. Central South Pacific, New Zealand Margin and South Pacific Gyre
 752 samples: Ho et al. (2014) and Jaeschke et al. (2017); Northern – Central Chilean Margin samples: Kaiser et al. (2015); Southern
 753 Chilean Margin and Drake Passage samples: Lamping et al. (2021) and this study. (E) – (F): Residuals for SST 0 – 50 m and Tsub 0
 754 – 200 m, with modern world ocean atlas-based temperatures (WOA05; Locarnini et al., 2006) subtracted from the calibrated
 755 temperatures. Green solid lines: standard error of $\pm 2.5^{\circ}\text{C}$ (SST^HKim) and $\pm 2.2^{\circ}\text{C}$ (Tsub^HKim). Red dashed lines: Calibration
 756 standard errors of $\pm 0.8^{\circ}\text{C}$ (SST^HKaiser) and $\pm 0.6^{\circ}\text{C}$ (Tsub^HKaiser).

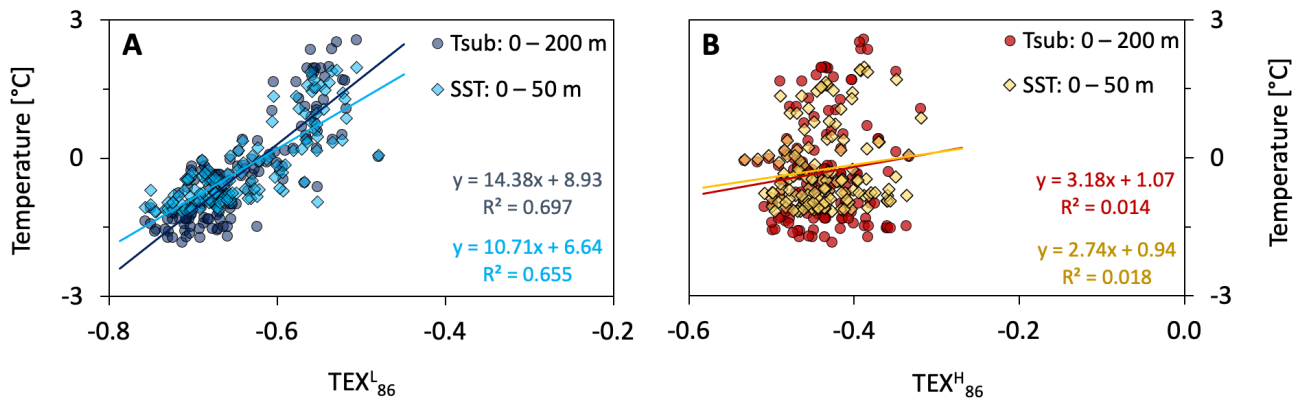
757



758

759 Figure 10: Map of GDGT [2]/[3]-ratios from our extended surface sediment sample set across different regions within the study
 760 area. SCM: Southern Chilean Margin; DP: Drake Passage; SAF: Subantarctic Front; PF: Polar Front.

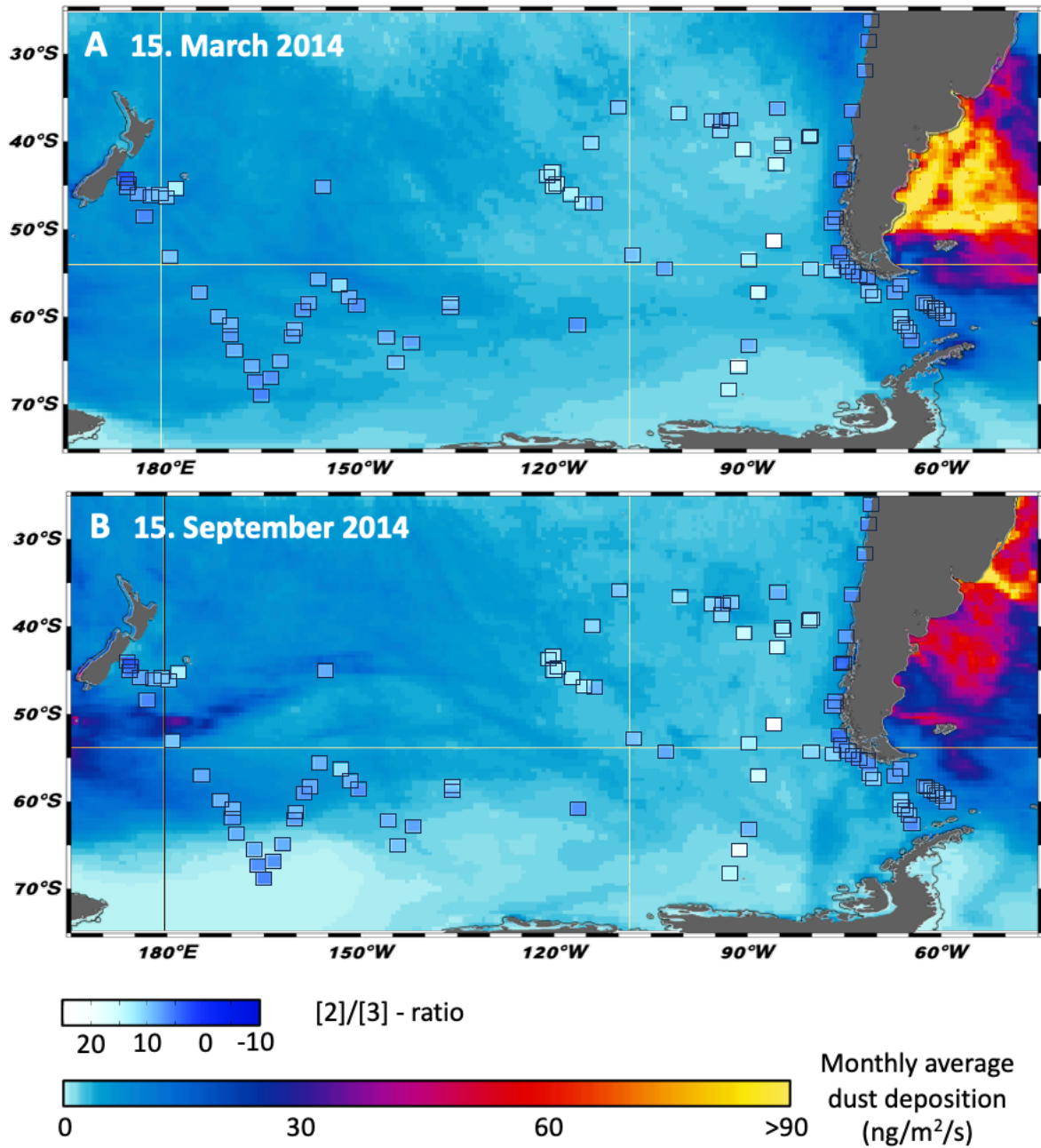
761



762

763 Figure 11: TEX₈₆^H and TEX₈₆^L Indices south of the SAF vs. modern WOA05 water temperatures. (A) TEX₈₆^L of all South Pacific
 764 samples; (B) TEX₈₆^H of all South Pacific samples.

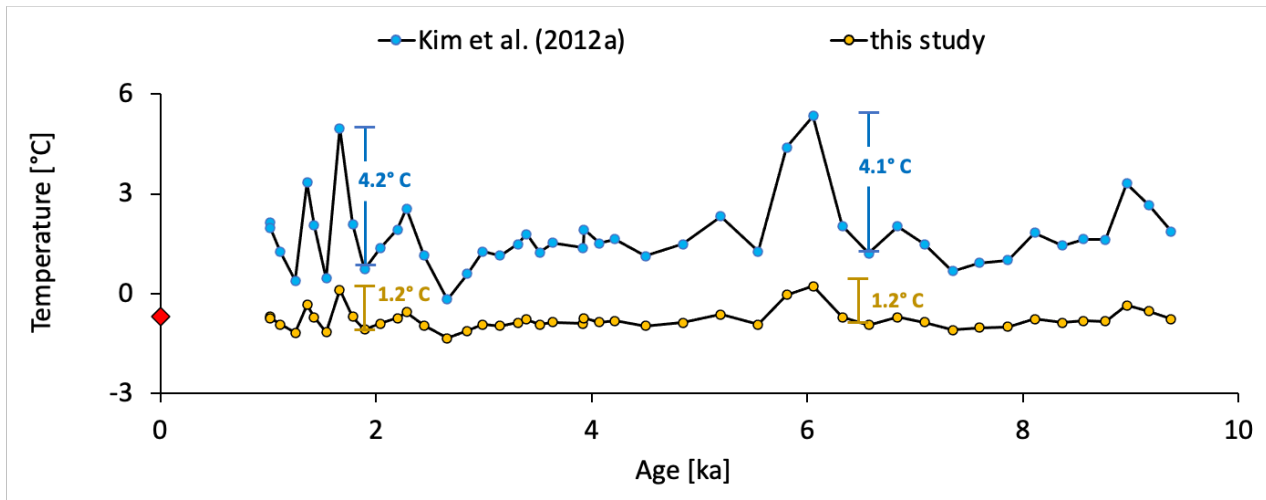
765



766

767 Figure 12: GDGT [2]/[3]-ratio on a map, showing total monthly average dust deposition (dry + wet) for the times (A) march 2014
 768 and (B) September 2014. Dust data were taken from NASA worldview (Global_Modeling_and_Assimilation_Office_(Gamo), 2015).

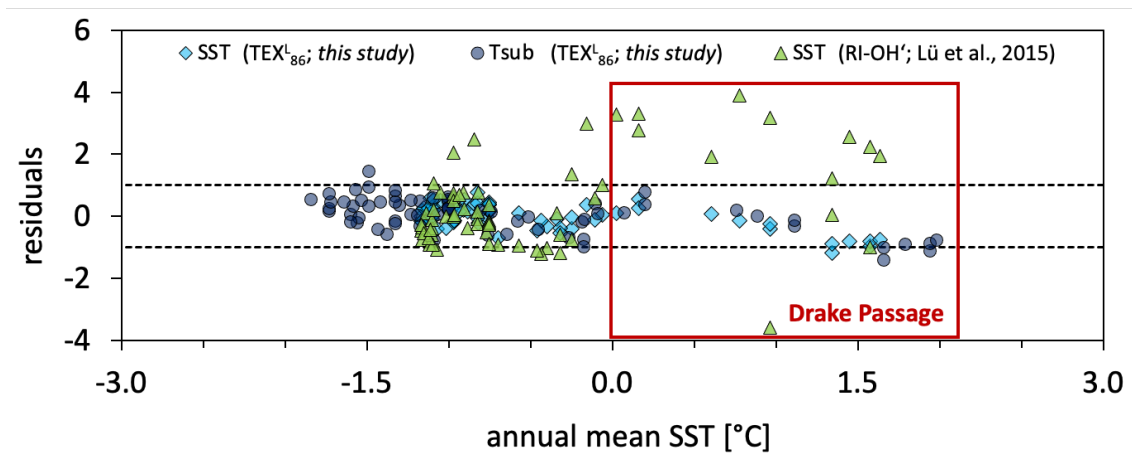
769



770

771 **Figure 13:** Comparison of core MD03-2601 (Kim et al., 2012b) with the temperature calibration T_{sub}^{L-Kim} (blue) and the new
 772 subsurface calibration of this study (yellow). Red dot marked the mean temperature of 0 – 200 m water depth at the coring site.

773



774

775 **Figure 14:** Residuals for SST 0 – 50 m and T_{sub} 0 – 200 m, with modern world ocean atlas-based temperatures (WOA05; Locarnini
 776 et al., 2006) subtracted from the calibrated temperatures. Black dashed lines mark the 1° C and -1° C isotherm, respectively.

777